Climatic control of the surface mass balance of the Patagonian Icefields

Tomás Carrasco-Escaff[1,2], Maisa Rojas[1,2], René Garreaud[1,2], Deniz Bozkurt[2,3], and Marius Schaefer[4]

[1]Department of Geophysics, University of Chile, Santiago, Chile
[2]Center of Climate and Resilience Research, University of Chile, Santiago, Chile
[3]Department of Meteorology, University of Valparaíso, Valparaíso, Chile
[4]Instituto de Ciencias Físicas y Matemáticas, Universidad Austral de Chile, Valdivia, Chile

Correspondence: Tomás Carrasco-Escaff (tcarrasco@dgf.uchile.cl)

Abstract. The Patagonian Icefields (Northern and Southern Patagonian Icefields) are the largest ice masses in the Andes Cordillera. Despite its importance, little is known about the main mechanisms that underpin the interaction between these ice masses and climate. Furthermore, the nature of large-scale climatic control over the surface mass variations of the Patagonian Icefields still remains unclear. The main aim of this study is to understand the present-day climatic control of the surface mass balance (SMB) of the Patagonian Icefields at interannual timescales, especially considering large-scale processes.

We modeled the present-day (1980-2015) glacioclimatic surface conditions for the southern Andes Cordillera by statistically downscaling the output from a regional climate model (RegCMv4) from a 10 km spatial resolution to a 450 m resolution grid, and then using the downscaled fields as input for a simplified SMB model. Series of spatially averaged modeled fields over the Patagonian Icefields were used to derive regression and correlation maps against fields from the ERA-Interim reanalysis.

Years of relatively high SMB are associated with the establishment of an anomalous low-pressure center near the Drake Passage, the Drake low, that induces an anomalous cyclonic circulation accompanied with enhanced westerlies impinging the Patagonian Icefields, which in turn leads to increases in the precipitation and the accumulation over the icefields. Also, the Drake low is thermodynamically maintained by a core of cold air that tends to reduce the ablation. Years of relatively low SMB are associated with the opposite conditions.

We found low dependence of the SMB on main atmospheric modes of variability (El Niño-Southern Oscillation, Southern Annular Mode), revealing a poor ability of the associated indices to reproduce interannual variability of the SMB. Instead, this study highlights the Drake Passage as a key region that has the potential to influence the SMB variability of the Patagonian Icefields.

1 Introduction

The Patagonian Icefields (Northern Patagonian Icefield (NPI) and Southern Patagonian Icefield (SPI)) are the most extensive ice bodies in the Andes Cordillera. Given their size, they play a significant role in modulating the local and regional environment, providing ecosystem processes such as climate regulation, gas regulation, and hydrologic cycles regulation, among others (Martínez-Harms and Gajardo, 2008; Dussaillant et al., 2012). Both icefields have been losing mass over the last decades

(Rignot et al., 2003; Malz et al., 2018; Minowa et al., 2021), and recent evidence shows that they are the primary contributors
25 to sea-level rise among all South American ice masses (Braun et al., 2019; Dussaillant et al., 2019). Overall, glaciers of the
Southern Andes have contributed approximately 3.3 mm of sea-level rise between 1961 and 2016 (Zemp et al., 2019). Despite
the importance of the Patagonian Icefields, little is known about the main mechanisms underpinning the interaction between
these ice bodies and climate, especially the large-scale climate processes that determine their surface mass balance (SMB) at
interannual timescales. This topic represents a significant issue for understanding the Patagonian Icefields' past, present, and
30 future evolution and, more generally, the southern Andean cryosphere.

The Patagonian Icefields spread over the 46-52ºS (Fig. 1), a latitudinal band influenced by the continuous passage of mid-
latitude systems embedded in an intense westerly flow (Trenberth, 1991; Berbery and Vera, 1996; Hoskins and Hodges, 2005).
The steep north-south oriented topography induces a substantial orographic enhancement of precipitation on the windward
side and a rain-shadow effect on the leeward side (Roe, 2005; Jobbágy et al., 1995; Garreaud et al., 2009). This generates a
35 temperate and hyper humid climate to the west of the Andean ridge and an arid and continental climate eastward (Paruelo
et al., 1998; Carrasco et al., 2002; Aravena and Luckman, 2009; Garreaud et al., 2013). Several authors reported a regional
warming trend in Patagonia (Rosenblüth et al., 1997; Rasmussen et al., 2007; Olivares-Contreras et al., 2019), whereas regional
precipitation trends are spatially inhomogeneous (Quintana and Aceituno, 2012; Aravena and Luckman, 2009; Garreaud et al.,
2013) For example, Boisier et al. (2018) report negative trends to the north of NPI, while González-Reyes et al. (2017) find
40 positive trends to the south of SPI.

The Patagonian climate is controlled primarily by the strength of the westerly winds (Garreaud et al., 2013). Garreaud et al.
(2013) find a high correlation between zonal wind and precipitation in western Patagonia at daily, monthly, and interannual
timescales. They also find a seasonal correlation between zonal wind and temperature, indicating that windy summers tend
to be colder than average and windy winters tend to be warmer than average. Consequently, modes of variability affecting
45 the westerly flow impact the Patagonian climate profoundly, such as the Southern Annular Mode (SAM), the leading mode
of extratropical Southern Hemisphere variability (Fogt and Marshall, 2020, for a review). This mode is characterized by an
equivalent barotropic, zonally symmetric structure involving exchanges of mass between the mid and high latitudes with
positive polarity associated with a strengthening and poleward shifting of the polar jet and negative polarity associated with a
weakening and equatorward shift of the polar jet (Rogers and Van Loon, 1982; Thompson and Wallace, 2000). Additionally,
50 subsidence and adiabatic warming occur in the troposphere on the equatorward side of the polar jet during the positive phase
of SAM, while opposite temperature anomalies maintain during the negative phase (Fogt and Marshall, 2020).

The circumpolar anomalies in westerly flow and tropospheric temperature exhibited during each phase of SAM lead to
corresponding anomalies in precipitation and surface temperature in Patagonia. In particular, southern South America (south
of 40ºS) exhibits warmer than average conditions during the positive phase of SAM, while opposite anomalies maintain during
55 the negative phase (Garreaud et al., 2009). In terms of precipitation, during the positive phase of SAM, northern Patagonia
exhibits dryer than average conditions, and southern Patagonia exhibits moister than average conditions, while the opposite
occurs during the negative phase (Garreaud et al., 2009). In fact, during the last decades, SAM has shown a significant positive
trend during the austral summer season associated primarily with ozone depletion and increase of greenhouse gases (Gillett and
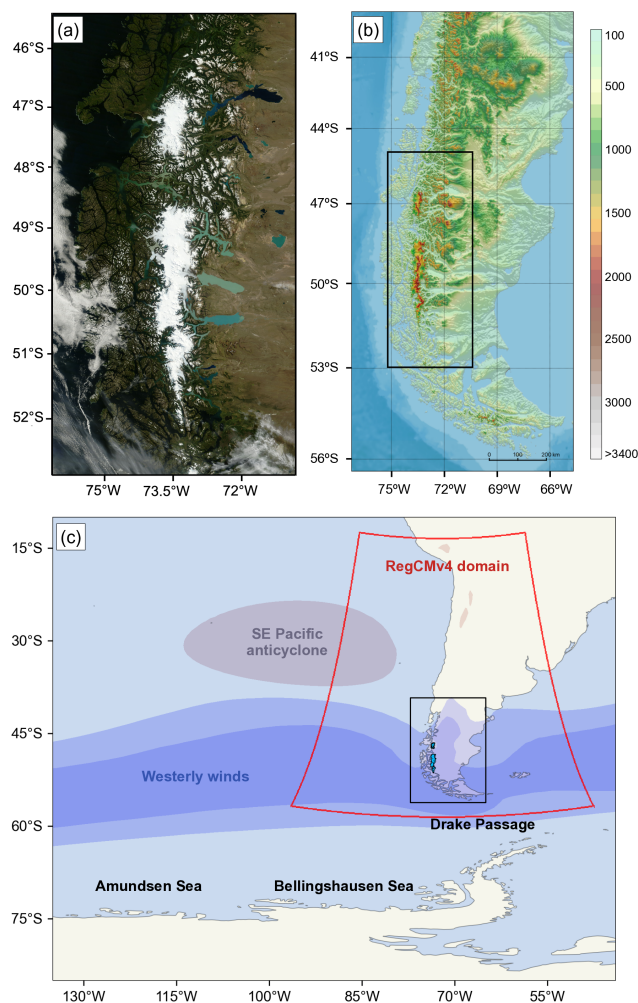
Figure 1. (a) Satellite image of Northern Patagonian Icefield and Southern Patagonian Icefield taken by the MODIS sensor on board the NASA's TERRA satellite on February 19, 2011. (b) Terrain elevation (m a.s.l.) of southern South America obtained from the digital elevation model ETOPO1 with 1 minute of arc resolution. The black box spans the area of panel (a). (c) Schematic of the main features of large-scale circulation near the Patagonian Icefields. The red polygon indicates the spatial domain used for running the RegCMv4 present-climate simulations. The black box spans the area of panel (b).

Thompson, 2003; Arblaster and Meehl, 2006), favoring dry conditions in northern Patagonia, mainly during summer (Boisier

60 et al., 2018).

Further modulation of the Patagonian climate is due to the El Niño-Southern Oscillation (ENSO), the Earth's largest source of year-to-year climate variability (Wang et al., 2017, for a review). During ENSO events, stationary Rossby wave trains are generated in response to deep convection generated by tropical sea surface temperature (SST) anomalies (Hoskins and Karoly, 1981; Karoly, 1989). These wave trains, identified in the Southern Hemisphere with the Pacific-South American pattern (Mo

and Higgins, 1998; Mo and Paegle, 2001), include anomalous anticyclonic circulation over the Amundsen–Bellingshausen Seas in the southeastern Pacific (Karoly, 1989) and are associated with enhanced blocking episodes in this region (Rutllant and Fuenzalida, 1991; Jacques-Coper et al., 2016; Demortier et al., 2021). These circulation anomalies can substantially influence the precipitation regime of southern South America. For instance, they have been related to a decrease in precipitation in western Patagonia during ENSO warm (El Niño) events, especially during summer, with the opposite conditions during cold (La Niña) events (Montecinos and Aceituno, 2003; Schneider and Gies, 2004; Weidemann et al., 2018; Garreaud, 2018; Agosta et al., 2020).

Furthermore, Cai et al. (2020) found slightly different spatial patterns of precipitation anomalies for Central Pacific ENSO events and Eastern Pacific ENSO events (Capotondi et al., 2015; Timmermann et al., 2018). The diversity of spatial patterns and intensities of SST anomalies in the tropical Pacific Ocean among ENSO events results in different atmospheric circulation responses (Taschetto et al., 2020), which in turn would affect the linkage between ENSO and Patagonian climate. Thus, even though dryer and warmer than normal conditions are expected during El Niño events, especially during summer, the net effect of ENSO on the Patagonian climate seems to depend on the specifics of each ENSO event.

The meteorological conditions over the Patagonian Icefields have a direct impact on the glaciological surface processes (e.g., snowfall, surface melting) that determine the gain (accumulation) and loss (ablation) of mass experienced by the glaciers. The SMB corresponds to the overall sum of the surface accumulation and surface ablation, i.e., the net surface gain of mass, over a certain period of time. Processes affected by the specific glacier dynamics, such as calving, or basal conditions, such as basal melting, represent possible sources of additional gain and loss of mass and determine, along with the SMB, the total mass balance of the glaciers, which, in turn, modulates their geometry. Unlike the total mass balance or the glacier geometry, the SMB integrates the direct interplay between glaciers and climate and thus represents a suitable study variable for assessing climate-cryosphere interaction.

Similar to many mountain regions in the world, the Patagonian Icefields show a lack of in situ climatic and glaciologic measurements due to difficult access and harsh environmental conditions. There are few measurement stations and short records available (Fig. S1), and this scenario hinders a robust assessment of glacier response to current climate conditions. Due to the inadequate observational network, various studies have tried to quantify the SMB of the Patagonian Icefields using different global gridded climate datasets (i.e., reanalysis), downscaling techniques (dynamical and statistical downscaling procedures), and SMB models of different complexity (Schaefer et al., 2013, 2015; Lenaerts et al., 2014; Mernild et al., 2017). Interestingly, all studies found positive trends in the SMB of the Patagonian Icefields and a positive SMB for the SPI. Nonetheless, none of them assess the interannual variability of the SMB nor its relationship with local and large-scale atmospheric processes.

On the other hand, even though several studies were published in the last two decades in which the mass loss of the Patagonian Icefield was quantified by remote sensing methods (Rignot et al., 2003; Willis et al., 2012a, b; Jaber et al., 2016; Malz et al., 2018; Foresta et al., 2018; Minowa et al., 2021), the methodological approach followed by these studies does not allow to obtain a quantitative assessment of SMB variability and its relationship with atmospheric processes. Thus, there is a substantial gap in understanding how atmospheric processes affect the SMB of the Patagonian Icefields, especially at interannual timescales.

100   Motivated by improving our knowledge about the climate-cryosphere interplay, this paper links the annual anomalies in the SMB of the Patagonian Icefields with local, regional, and large-scale climate anomalies. The main goal of this work is to understand the present-day climatic control of the SMB of the Patagonian Icefields at interannual timescales, especially considering large-scale processes. Understanding the mechanisms behind year-to-year changes in the SMB is an essential requirement for deepening the comprehension of the climate processes responsible for past, present, and future trends of the

105   SMB of the Patagonian Icefields and an important opportunity for future development of diagnostic and prognostic tools. To achieve our goal, we simulate present-day glacioclimatic surface conditions for the southern Andes Cordillera using a simplified SMB model forced with a high-resolution regional climate model simulation. The paper is structured as follows: in Sect. 2, we describe the study area, data, and methods used in the study. In Sect. 3 and Sect. 4, we present the results and discussion, respectively. Finally, in Sect. 5, we present the conclusions of our work.

110   2   Study Area, Data, and Methodology

2.1   Study Area

The study area comprises the Patagonian Icefields. They spread over a latitudinal band of 46-52º S and include the NPI and the SPI (Fig. 1). The NPI locates between 46º30' S and 47º30' S and covers a total ice area of 3953 km^2 (Rivera et al., 2007). It elongates in the north-south direction with an axis near the 73º30' W, extending ~100 km in length and 40-45 km in width

115   (Aniya, 1988). It shows a steep topography with terrain elevation values increasing eastward in most parts of the icefield area, reaching the sea level at the west margin and a maximum of 3970 m a.s.l (above sea level). at the summit of Mount San Valentín. Characteristic terrain elevation values are 1000 m a.s.l. for the west side and 1500 m a.s.l. for the east side (Warren and Sugden, 1993). The NPI is composed of 38 glaciers larger than 0.5 km^2 (Dussaillant et al., 2018).

    The SPI locates between 48º20' S and 51º30' S and covers a total ice area of 12514 km^2 (Casassa et al., 2014). It extends

120   ~350 km in length and generally 30-40 km in width, with the narrowest part only 8 km wide (Aniya et al., 1998). This icefield contains a central plateau lying between the 1400-2000 m a.s.l. with terrain elevation values decreasing southward. The SPI reaches its topographic maximum at Volcán Lautaro with a peak of 3607 m a.s.l. It is composed of 48 main outlet glaciers (Aniya et al., 1998).

2.2   Data

125   To overcome the lack of observational surface data in the area, we modeled present-day glacioclimatic surface conditions for the southern Andes cordillera. First, we obtained the simulated meteorological fields from a regional climate model (RegCMv4) at 10 km spatial resolution and 3 h temporal resolution for the period 1980-2015 (Bozkurt et al., 2019). The regional climate simulation setting consisted of two nested domains at 0.44º (~50 km) and 0.09º (~10 km) spatial resolutions and 23 sigma levels. Initial and boundary conditions for the mother domain were provided by ERA-Interim reanalysis at 6 h temporal
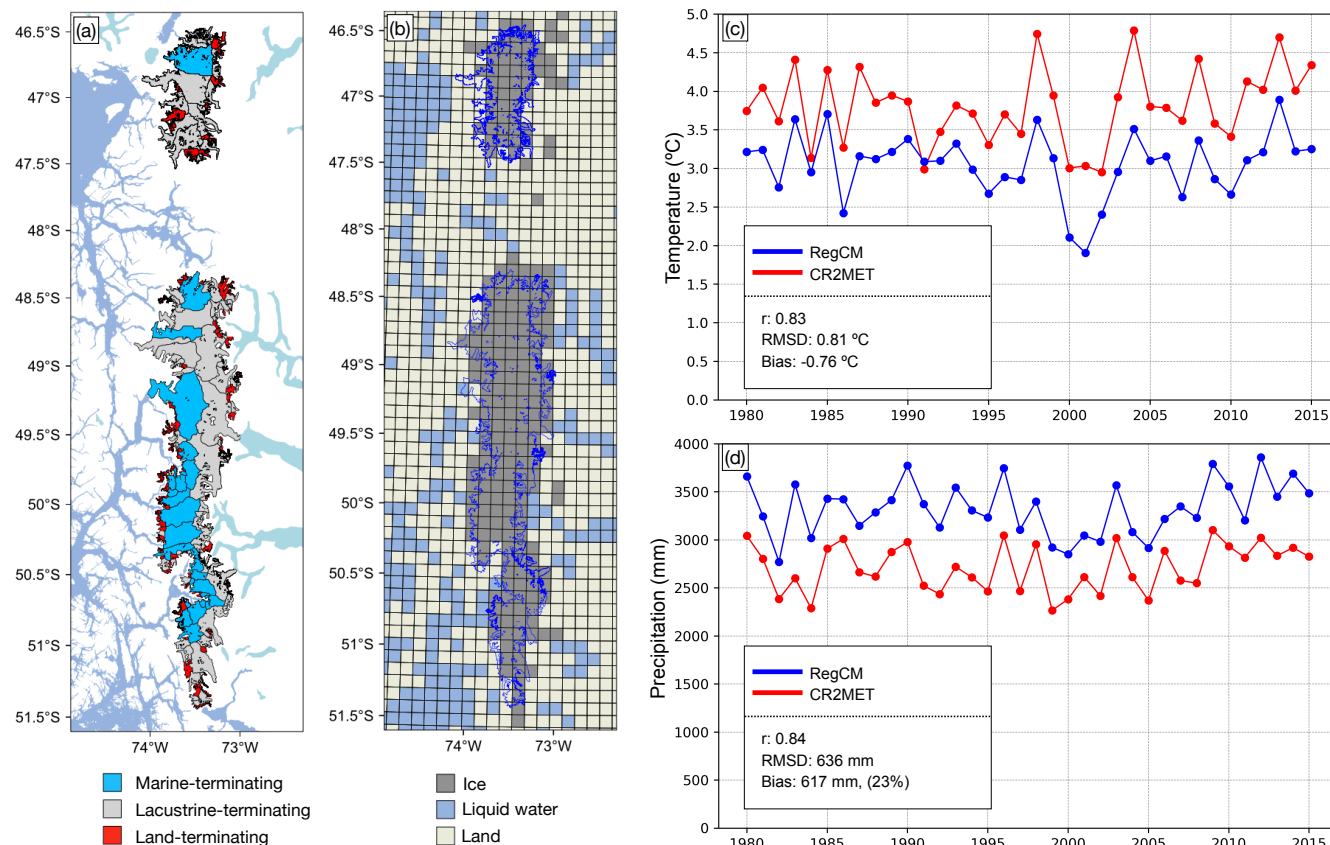
Figure 2. (a) Patagonian Icefields together with their glacier divides and type of terminus. (b) The RegCMv4 grid (∼10 km spatial resolution), the model land use (grid box colors) and the NPI and SPI outlines (blue contours). (c) Comparison of annual mean temperature time series (box at 46-52º S and 72.5-74.5º W) using RegCMv4 data and CR2MET data. (d) Same as (c) but for accumulated annual precipitation.

130 resolution and 0.75º spatial resolution, including SST fields. More information about the RegCMv4 and simulations can be found in Bozkurt et al. (2019)

Before running the glaciological model, we verified the RegCM simulated meteorological fields with a high-resolution (CR2MET, 0.05º spatial resolution) gridded meteorological dataset (version 1.4.2 of precipitation data and version 1.3 of temperature data). In this manner, we evaluate RegCM4 performance in capturing near-surface temperature and precipitation

135 variability in the Patagonian Icefields. The CR2MET dataset is based on in situ observations of precipitation and temperature for the territory of continental Chile, covering the period 1979–present. The CR2MET product is partly based on a statistical downscaling of ERA-Interim reanalysis. In terms of precipitation, the dataset considers the local topography, which is defined by a set of calibrated parameters with local rainfall observations. Similarly, land surface temperature estimates from MODIS satellite retrievals are considered in the statistical downscaling approach and near-surface temperature provided by ERA-

140 Interim. More detailed information about the CR2MET can be found in Alvarez-Garreton et al. (2018).

Elevation terrain data were obtained from the NASA Shuttle Radar Topography Mission Global 3 arc second sub-sampled (STRMGL3S V003; hereafter STRMv3) distributed by NASA Making Earth System Data Records for Use in Research Environment (MEaSUREs) SRTM (NASA JPL, 2013), which has a 3" horizontal resolution (∼90 m). Additionally, glacier extent data were obtained from the Randolph Glacier Inventory Version 6 (RGIv6; RGI Consortium, 2017). The RGIv6 is a globally complete inventory of glacial outlines. It has a collection of vector data that describes the geometry associated with various glaciers and other types of information such as area, mean elevation, and type of term. It is a supplement to the GLIMS initiative (Global Land Ice Measurements from Space) that aims to be a photograph of the glacier extension in the world at the beginning of the 21st century.

To assess large scale patterns associated with SMB anomalies, data from several climatic variables for the period between 1980-2015 were taken from the European Centre for Medium-Range Weather Forecasts (ECMWF) Reanalysis (ERA-Interim) dataset with a grid spacing of 0.75º × 0.75º (Dee et al., 2011) including surface air temperature (SAT), zonal and meridional wind (u and v, respectively), mean sea level pressure (MSLP), geopotential height (Z), and SST. Also, outgoing longwave radiation (OLR) flux at the top of the atmosphere data was taken from the NOAA Climate Data Record (CDR) Program, with a grid spacing of 2.5º x 2.5º (Lee and NOAA CDR Program, 2011)

2.3 Methodology

We first statistically downscaled near-surface air temperature, precipitation, and surface downward solar radiation fields obtained from RegCMv4 to a 450 m resolution grid. After that, we used these meteorological fields as input for a simplified SMB model. Lastly, we spatially unweighted averaged the meteorological forcing and the glaciological over the Patagonian Icefields area to derive the time series of the modeled fields. Note that only grid points within a mask file of the Patagonian Icefields were used for spatial-average comparisons. The annual time series of the modeled fields were computed using hydrological years from April to March. Similarly, we calculated the modeled fields' winter and summer time series, with winters spanning April to September and summers from October to March.

2.3.1 Statistical downscaling of the RegCMv4 output

The RegCMv4 DEM digital elevation model (DEM) tends to underestimate the terrain elevation when compared with the SRTMv3 DEM, especially at higher elevations, both in the NPI and the SPI (Fig. S2). In order to avoid biases in near-surface temperature and precipitation due to elevation biases, we corrected the near-surface temperature and precipitation RegCMv4 model output accounting for the biases in the RegCMv4 DEM.

To do so, we first constructed a DEM resulting from the averaged SRTMv3 DEM at every five grid points (∼450 m spatial resolution) and used this as the default model DEM. This spatial resolution was selected after performing a sensitivity analysis (Carrasco-Escaff, 2021). We then statistically downscaled the RegCMv4 main surface atmospheric output (near-surface air temperature, precipitation, and surface downward solar radiation) from 10 km spatial resolution to the 450 m resolution grid. Regarding the temporal resolution, each field remained at a 3 h resolution.

The statistically downscaling process started with the bilinear interpolation of the fields onto the RegCMv4 DEM to remap data from a 10 km resolution to a 450 m grid resolution of the default model DEM. Then, we performed altitudinal corrections

175 for temperature and precipitation. In the case of temperature, we applied a constant lapse rate equal to the environmental lapse rate (6.5 ℃ km^{-1}). In this way, we computed the near-surface temperature every 3 h according to:

$$T = T_{\mathrm{bil}} - \mathrm{LR} \cdot (z - z_{\mathrm{bil}}) \tag{1}$$

where T is the downscaled near-surface temperature, T_{bil} is the 450 m bilinearly interpolated RegCMv4 near-surface temperature, LR = 6.5 ℃ km^{-1} is the lapse rate, z is the model reference DEM, and z_{bil} is the 450 m bilinearly interpolated RegCMv4

180 DEM. In the case of precipitation, we used the following equation at every 3 h:

$$P = P_{\mathrm{bil}} \cdot (1 + \mathrm{PG} \cdot (z - z_{\mathrm{bil}})) \tag{2}$$

where P is the statistically downscaled precipitation, P_{bil} is the 450 m bilinearly interpolated RegCMv4 precipitation, and PG = 0.05% m^{-1} is the precipitation gradient (as in Schaefer et al., 2013, 2015). Finally, we downscaled the surface downward solar radiation by performing bilinear interpolation on the RegCMv4 original field.

185 ### 2.3.2 SMB model

We used the statistically downscaled fields as input for a simplified SMB model. The SMB model output consists of accumulation, ablation, and SMB fields with 3 h temporal resolution and 450 m spatial resolution. The accumulation (c) at every grid cell is defined as the solid part of precipitation (P) and computed as:

$$c = q \cdot P \tag{3}$$

190 where q is the fraction of precipitation that falls as snow and determined by the near-surface temperature (T) of the grid cell according to:

$$q = \begin{cases} 0, & \text{if } 2\,℃ \leq T \\ \frac{2\,℃ - T}{2\,℃}, & \text{if } 0\,℃ \leq T < 2\,℃ \\ 1, & \text{if } T < 0\,℃ \end{cases} \tag{4}$$

The ablation (a) at every grid cell is represented by melting, and it is computed using a simplified energy balance model in which the sum of longwave radiation and turbulent fluxes is approximated by a linear function in temperature (Oerlemans,

195 2001). First, the surface energy flux (ψ) is calculated according to:

$$\psi = (1 - \alpha) \cdot R + c_0 + c_1 \cdot T \tag{5}$$

where α is the surface albedo, R is the surface downward solar radiation, T is the near-surface temperature in ℃, and c_0 and c_1 are the calibration parameters. Then, the ablation is computed as:

$$a = \begin{cases} \frac{\psi}{L_m \rho_w} \cdot 10800 \text{ s}, & \text{if } \psi > 0 \\ 0, & \text{if } \psi \leq 0 \end{cases} \tag{6}$$

200 where $L_m = 333.55 \times 10^{-3}$ J kg^{-1} is the latent heat of fusion and $\rho_w = 1000$ kg m^{-3} is the liquid water density.

The SMB model assigns one of three types of soil to every grid cell: snow, firn, and ice. Each type of soil has a specific albedo (snow albedo is 0.85, firn albedo is 0.55, and ice albedo is 0.35), and they were taken from Cuffey and Paterson (2010). In the SMB model, every grid cell consists of a column of ice at the bottom, possibly followed by a column of firn and possibly by a column of snow. At every 3 h and for each grid cell, the SMB model calculates the accumulation added to the column of

205 snow. Then, the SMB model computes the ablation, and the model simulates the melting of the (possible) snow, followed by the (possible) firn and the ice. Finally, the SMB is computed at every 3 h and for each grid cell according to:

$$b = c - a \tag{7}$$

At the end of each summer season (1 April), the mass of firn in the firn column turns into ice, and the mass of snow in the snow column turns into firn. Initially, each grid cell consists of only a column of ice (infinitely deep), and the SMB model was

210 forced with the downscaled climatological conditions obtained from the RegCMv4 for five years before feeding it with the true RegCMv4 downscaled fields.

2.3.3 Calibration and sensitivity to possible biases in the mean state

The parameters c_0 and c_1 were calibrated using the SMB estimations for the NPI and the SPI from Minowa et al. (2021). These are the only known estimates based on an observational approach covering both the NPI and the SPI in an icefield-wide sense.

215 Minowa et al. (2021) estimated a -1.5 Gt yr^{-1} SMB annual rate for the NPI in the period 2000-2019 and an 11.5 Gt yr^{-1} SMB annual rate for the SPI in the same period. Even though the temporal coverage of our SMB model ends in 2015, we calibrated the parameters c_0 and c_1 for the period 2000-2015 to compare with the values reported by Minowa et al. (2021).

To calibrate the model parameters, we ranged c_0 from -48 to 48 Wm^{-2} every 1.0 Wm^{-2} and c_1 from 9.5 to 11.5 Wm^{-2}°C^{-1} every 0.5 Wm^{-2}°C^{-1}. For every pair of values (c_0, c_1), we computed the annual rate of SMB for the NPI and the SPI between

220 1 April 2000 and 31 March 2015. Then, we compared it with the estimates from Minowa et al. (2021) for the period 2000-2019. The closest value for the NPI was found using the calibration parameters $c_0 = -6$ Wm^{-2} and $c_1 = 9.5$ Wm^{-2}°C^{-1}, producing an SMB annual rate of -1.48 Gt yr^{-1}. Meanwhile, the closest value for the SPI was reached using the values $c_0 = 21$ Wm^{-2} and $c_1 = 9.5$ Wm^{-2}°C^{-1}, giving an SMB annual rate of 11.41 Gt yr^{-1}.

The absence of observational data in the study area in an icefield-wide sense imposes a limitation on validating the SMB

225 model output. To overcome this limitation, we conducted a sensitivity analysis to determine whether possible biases in the mean state of the meteorological input fields could lead to different results in terms of the interannual variability of the SMB of the Patagonian Icefields. A brief evaluation of the simulated mean annual climate by RegCMv4 with respect to CR2MET is given in Fig. 2c, d. Overall, it can be stated that the model well captures the interannual variability. Nonetheless, there exist systematic colder (mean bias of -0.76 °C) and wetter estimates (23% mean bias) compared to CR2MET, which can be

230 associated with biases of boundary conditions and the regional climate model itself.

Therefore, we added an offset T_0 to the near-surface temperature ranging from -1.5 to 1.5 °C every 0.5 °C and weighted the precipitation with a factor P_0 ranging from 0.8 to 1.2 every 0.1. For each pair of values (T_0, P_0), we rerun the SMB model and
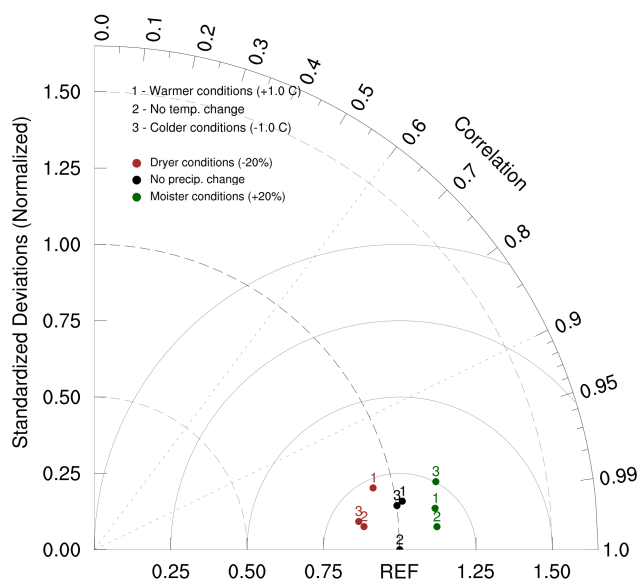
Figure 3. Sensitivity of modeled SMB interannual variability to possible biases in the mean state of meteorological variables. Each point on the diagram represents a different combination of possible biases in the mean value of near-surface temperature (numbers above the markers) and precipitation (marker colors). The angle of the point represents the correlation (Pearson's r coefficient) between the annual time series of modeled SMB without changes in the mean state of the meteorological variables (reference series) and annual time series of modeled SMB obtained by altering the mean state of the temperature and/or precipitation before the SMB model is run. The radius of the point corresponds to the ratio of the standard deviation of the SMB time series obtained by altering the mean state of the temperature and/or precipitation to the standard deviation of the reference series.

obtain an annual series of SMB for the Patagonian Icefields. Then we compute the Pearson's r coefficient between this series and the original one ($T_0 = 0.0$ °C and $P_0 = 1.0$) and also calculate its standard deviation. With these metrics, we created the

235   Taylor diagram shown in Fig. 3. It shows that even though we cannot validate the mean state of the meteorological input and glaciological output, we can assure that possible biases in the mean state of these fields do not affect the interannual variability of the SMB, which is the main focus of our work.

2.3.4   Dependence of annual variations in SMB on annual variations in meteorological variables

We determined the degree of dependence of the interannual variability of the SMB on the interannual variability of the down-

240   scaled fields of temperature, precipitation, and insolation. To do this, we conducted experiments in which we (i) removed the variability of a period $T \geq 1$ yr for a specific meteorological field (e.g., precipitation); (ii) remained the other meteorological fields unmodified (e.g., temperature and solar radiation); (iii) rerun the SMB model; and (iv) computed the time series of the spatially averaged fields of SMB using the new output.

Next, we calculate the squared correlation (R^2) between the original SMB time series and the SMB time series computed

245   from the new output at annual, winter, and summer timescales (we performed the same procedure in the case of accumulation

Variability $T \geq 1$ yr removed from	Time correlation	SMB	Accumulation	Ablation
Precipitation	Annual	26 %	0 %	95 %
	Winter	0 %	9 %	98 %
	Summer	67 %	15 %	95 %
Temperature	Annual	45 %	84 %	9 %
	Winter	74 %	93 %	3 %
	Summer	40 %	72 %	19 %
Insolation	Annual	95 %	100 %	81 %
	Winter	99 %	100 %	93 %
	Summer	95 %	100 %	81 %

Table 1. Results from the sensitivity experiment designed to assess the degree of dependence of the variations of SMB, accumulation and ablation on the variations of the meteorological variables. The percentages indicate the R2 metric calculated between the original and the modified time series. A high value of this metric is interpreted as a low degree of dependence of the glaciological variable on the meteorological variable whose variability of period equal to or greater than one year has been removed.

and ablation). We interpreted a high (low) value of R^2 as a low (high) degree of dependence in terms of interannual variability. For example, after removing the interannual variability of precipitation, the R^2 value between the resulting SMB and the original SMB is 0.26, which indicates a strong dependence of the interannual variability of the SMB on the interannual variability of precipitation. The results are tabulated in Table 1.

250 2.3.5 Large-scale climate indices

We determined the correlation between the modeled time series and several large-scale climate indices in order to assess the influence of the main modes of interannual variability on the SMB of the Patagonian Icefields. To characterize ENSO activity we used the monthly values of SST averaged over the Nino1+2 and the Nino3.4 regions (see Fig. 4) obtained from the NOAA Climate Prediction Center (CPC, https://psl.noaa.gov/data/climateindices/list/). Additionally, we used the Central Pacific (CP)

255 and Eastern Pacific (EP) ENSO indices to account for ENSO diversity (Kao and Yu, 2009; Yu et al., 2012). To obtain the spatial pattern and temporal index of EP ENSO, SST anomalies regressed with the Nino4 index are removed from total SST anomalies before performing Empirical Orthogonal Function (EOF) analysis. The same approach is used for computing the CP index but using the Nino1+2 index instead. To characterize SAM activity we used the AAO index obtained from NOAA CPC. We used monthly means of daily values, which are constructed by projecting the daily height anomalies at 700 hPa poleward 20º S onto

260 the leading mode of EOF analysis of monthly mean 700 hPa height during the 1979-2000 period.
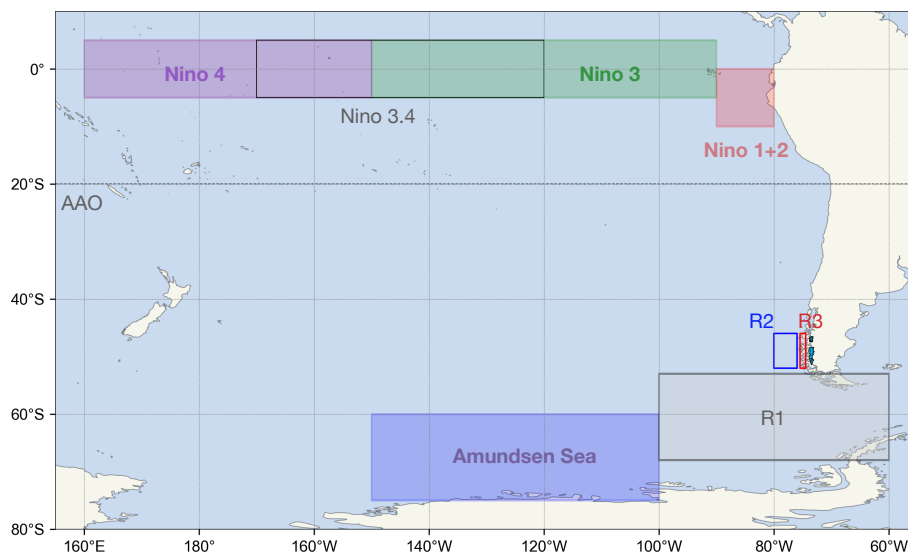
Figure 4. Regions used for the construction of climate indices.

Additionally, we constructed custom indices in order to assess the covariability between the modeled variables and some climatic variables averaged over specific regions of interest (Fig. 4). We spatially averaged the monthly values of the ERA-Interim geopotential height at 300 hPa and air temperature at 850 hPa in a box near the Drake Passage spanning the 68-53º S in latitude and 100-60º W in longitude (box R1 in Fig. 4). We did the same with the SST of the Pacific Ocean next to central

265 Patagonia (box R2 in Fig. 4, at 52-46º S and 80-76º W) and with the zonal wind at 850 hPa impinging central Patagonia (box R3 in Fig. 4, at 52-46º S and 75.5-74.5º W). We named these time series Z300 Drake, T850 Drake, SST-R2, and U850-R3, respectively.

3   Results

3.1   Mean values and covariability

270 Fig. 5 shows the annual time series of SMB, accumulation, ablation, precipitation, temperature, and insolation, calculated as the spatial average of each field over both icefields. The mean values of these time series are tabulated in Table 2 and their standard deviations in Table S1. The annual SMB averages 469 ± 537 mm w.e. (mean $\pm$ std. dev.; w.e. stands for water equivalent). During winter (April to September), the SMB increases up to 1806 ± 331 mm w.e., while during summer (October to March) it decreases down to -1336 ± 428 mm w.e. The annual precipitation averages 6430 ± 536 mm w.e., and about 74% of the

275 precipitation falls as snow. Mean winter and summer precipitation values are very similar, yet mean winter accumulation is 1.24 times the mean summer accumulation. Ablation shows a greater seasonal difference with a summer mean value of 4.17 times the winter mean value. The mean annual temperature (-1.82 ± 0.37 ºC) is below the freezing point, averaging $-3.44 \pm$
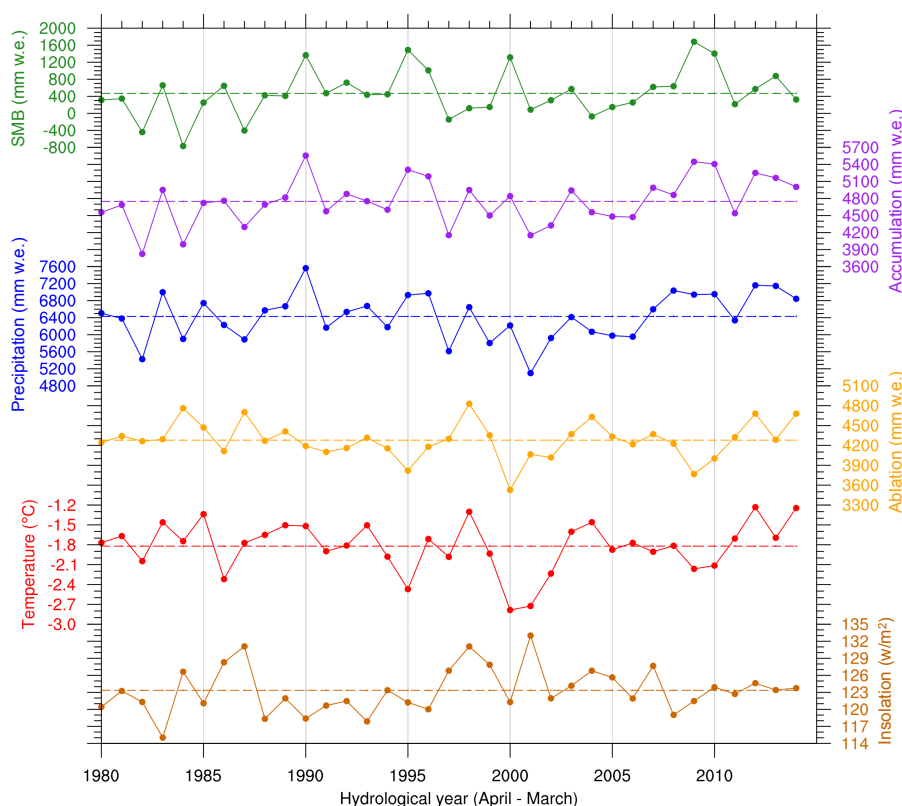
Figure 5. Annual (April to March) time series of spatially averaged (over the area of the Patagonian Icefields) fields of (from top to bottom) SMB, accumulation, accumulated precipitation, ablation, mean near-surface temperature and mean insolation. Each segmented line indicates the mean value of the series.

Mean values	SMB	Accumulation	Ablation	Precipitation	Temperature	Insolation
Units	mm w.e.	mm w.e.	mm w.e.	mm w.e.	ºC	Wm^{-2}
Annual	469	4748	4279	6430	-1.82	123
Winter	1806	2633	827	3214	-3.44	56
Summer	-1336	2115	3452	3217	-0.20	191

Table 2. Mean values of the annual (April to March), winter (April to September) and summer (October to March) time series of the spatially averaged modeled fields.

0.57 ºC and -0.20 ± 0.42 ºC during winter and summer, respectively. Finally, the annual insolation averages $123 \pm 4 \ \text{Wm}^{-2}$ with a summer mean value of 3.43 times the winter mean value.

Annual corr.	SMB	Accumulation	Ablation	Precipitation	Temperature	Insolation
SMB	1.00	-	-	-	-	-
Accumulation	0.87^*	1.00	-	-	-	-
Ablation	-0.68^*	-0.23	1.00	-	-	-
Precipitation	0.69^*	0.90^*	-0.02	1.00	-	-
Temperature	-0.25	0.19	0.78^*	0.45^*	1.00	-
Insolation	-0.44^*	-0.33	0.37^*	-0.53^*	-0.19	1.00

Table 3. Correlation (Pearson's r coefficient) between pairs of annual (April to March) time series of the spatially averaged modeled fields.
(*) Statistically significant value at a significance level of 5%.

280   Correlation (Pearson's r coefficient) between pairs of time series was computed (Tables 3, S2 and S3), and hypothesis testing was performed at a significance level of 5% ("*" corresponds to statistically significant values). Results show that the annual SMB is highly and positively correlated with the annual accumulation ($r = 0.87^*$) and negatively correlated with the annual ablation ($r = -0.69^*$). During winter, the correlation between the SMB and the accumulation increases ($r = 0.94^*$), while the correlation between SMB and the ablation decreases and becomes statistically non-significant. During summer, the

285   correlation between the SMB and the accumulation equals in magnitude the correlation between the SMB and the ablation ($r = -0.90^*$). Among the modeled meteorological variables, the annual SMB is found to have the largest correlation with the annual precipitation ($r = 0.69^*$), followed by annual insolation ($r = -0.44^*$) and annual temperature ($r = -0.25$) (see Table 3). The same order is also evident in winter, yet, the correlation between the SMB and temperature is found to be largest in summer. Additionally, results show that the modeled meteorological variables are correlated with each other. For instance, the

290   annual precipitation and insolation show a moderate but significant correlation ($r = -0.53^*$), while annual temperature and insolation show no significant correlation ($r = -0.19$) (Table 3). Annual temperature and precipitation are positively correlated, reaching a value of $r = 0.45^*$. During winter, this correlation increases ($r = 0.61^*$), while, during summer, it becomes almost null ($r = 0.05$).

3.2   Local-scale control over the SMB

295   First, we assessed the local-scale control over the SMB from the results of the sensitivity experiments described in Sect. 2.3.4 and tabulated in Table 1. We use the squared correlation R^2 metric to measure the degree of dependence of the SMB interannual variability on a specific meteorological variable. A high (low) value of R^2 is interpreted as a low (high) degree of dependence. The results show almost no dependence of the annual variations of the SMB on the annual variations of insolation ($R^2 = 95\%$). Furthermore, an almost null degree of dependence of the variations of the SMB on variations of insolation is maintained when

300   we analyze winter-to-winter variations ($R^2 = 99\%$) and summer-to-summer variations ($R^2 = 95\%$). The annual variations of SMB show a high dependence on the annual variation of temperature and precipitation, and this dependency is found to be

Linear regression	SMB	Accumulation	Ablation	Precipitation	Temperature	Insolation
Units			mm w.e./std. dev.		ºC/std. dev.	Wm^{-2}/std. dev.
Annual	537*	351*	−186*	368*	−0.09	−1.72*
Winter	200*	188*	−12	212*	0.04	−1.14*
Summer	336*	163*	−173*	156*	−0.23*	−2.31*

Table 4. Linear regression of the annual (April to March) time series of the spatially averaged SMB with the annual (April to March), winter (April to September) and summer (October to March) time series of the spatially averaged fields of SMB, accumulation, ablation, accumulated precipitation, mean temperature and mean insolation. (*) Statistically significant value at a significance level of 5%.

larger on annual precipitation ($R^2 = 26\%$) compared to that on annual temperature ($R^2 = 45\%$). The same order of dependency is also evident in winter. Nonetheless, summer temperature variations appear to have larger influences on the variations of SMB than summer precipitation variations. These results show that the local-scale control over the SMB is exerted primarily by the

305   temperature and precipitation. Precipitation exerts the primary control at annual and winter timescales, and the temperature does it at the summer timescale.

Next, we assessed the local-scale control over the SMB using regression analysis on the time series of spatially averaged fields over the Patagonian Icefields. These time series were regressed onto the annual time series of the spatially averaged field of SMB. This allows us to estimate the characteristic variation of each modeled glaciological and meteorological variable

310   associated with a positive or negative anomaly in annual SMB. The results of the regression analysis are shown in Table 4. For simplicity, we analyze a year when the SMB is one standard deviation above the mean value (the analysis extends linearly to other cases). An annual SMB anomaly of 537 mm w.e. is associated with an annual accumulation anomaly of 351 mm w.e. and an annual ablation anomaly of -186 mm w.e. Regarding seasonal differences, years with relatively large SMB are associated with higher than average winter and summer accumulation values and lower than average summer ablation values.

315   The winter accumulation anomaly is 1.15 times the summer accumulation anomaly but the summer ablation anomaly is more than 14 times the winter ablation anomaly. As a result, when grouping contributions by process, the annual SMB anomalies are primarily explained by accumulation anomalies, while when grouping by season, the summer anomalies in the glaciological processes account for most of the annual SMB anomalies.

The same analysis (i.e., the SMB is one standard deviation above the mean value) yields an increase of winter precipitation

320   of 212 mm w.e., whereas an almost null and not statistically significant variation in winter temperature. During summer, there is an increase of precipitation of 156 mm w.e. and a variation in temperature of -0.23 ºC. Thus, our results suggest that years with higher than average SMB are related to wetter than normal annual conditions and colder than normal summer conditions, while years with lower than average SMB are associated with the opposite.

3.3 Regional-scale control over the SMB

325   To assess the regional scale control over the SMB, we first computed the regression of the annual SMB with the annual precipitation, near-surface temperature, and horizontal wind (at 10 m above ground level and 700 hPa). Results are shown in Fig. 6a, c. For simplicity, we analyze the years when the SMB is above the mean value (the analysis extends linearly to other cases). Positive anomalies of annual SMB are associated with an intensification of the westerly winds impinging the Austral Andes, a regional cooling in the south of South America and over the Pacific Ocean adjacent to Patagonia, and an increase

330   (decrease) of the precipitation to the west (east) of the Andean ridge. The cooling is stronger over the Pacific Ocean adjacent to central and north Patagonia and northeast of the Patagonian Icefields. The increase in precipitation reaches the highest values in central-western Patagonia, with a maximum over the Patagonian Icefields. Over the Pacific Ocean adjacent to Patagonia, the circulation acquires anticyclonic vorticity to the north and cyclonic vorticity to the south, both at the near-surface level and at the 700 hPa pressure level. Some differences in horizontal wind anomalies are evident when comparing near-surface level and

335   at 700 hPa pressure level due to the topographic blocking imposed by the Andes.

We also computed latitudinal profiles of regressions of the annual SMB with the mean annual fields of zonal wind, geopotential height, and air temperature at a longitude of 80 ºW. Results are shown in 6b, d. The intensification of the westerly winds during years of relatively high SMB comprises the southern tip of the Andes, extending from near 38 ºS to near 60 ºS and maximizing near 50 ºS. At altitude, the positive zonal wind anomaly extends throughout the entire troposphere and reaches

340   its maximum around 300 hPa, between cores of high and low anomalous geopotential height, in a region where the pressure gradient is maximum. In turn, these cores of anomalous geopotential height are located in regions where the magnitude of the temperature gradient is maximum, resembling a thermal wind balance. Interestingly, the anomalous cold region below the core of low anomalous geopotential height extends to the lower troposphere and comprises the latitudinal band where the Patagonian Icefields are located. This suggests that during years of relatively high SMB, the reinforcement of the westerlies wind

345   impinging Patagonia and the temperature anomaly observed in the Patagonian Icefields could be linked to the same mechanism.

Regarding seasonal differences, years with SMB above the average shows a stronger circulation and a more pronounced precipitation change during winter than summer (Figs. 7, 8). Also, these years are associated with a pronounced summer cooling over the south of South America and the adjacent Pacific Ocean (Fig. 8c), while correlations with winter near-surface temperature are virtually null. The latitudinal profiles also show a stronger reinforcement of the westerly winds during winter

350   than summer (Fig. 7b), associated with more pronounced cores of anomalous geopotential height (Fig. 7d). Nonetheless, during summer, the low-pressure structure appears displaced northward, especially in the lower troposphere (Fig. 8d). A more intense cooling of the anomalous cold region tends to concentrate in the lower troposphere (1000 to 700 hPa), which could explain the summer cooling observed along the Patagonian Icefields.

Annual SMB projected onto annual fields of selected variables
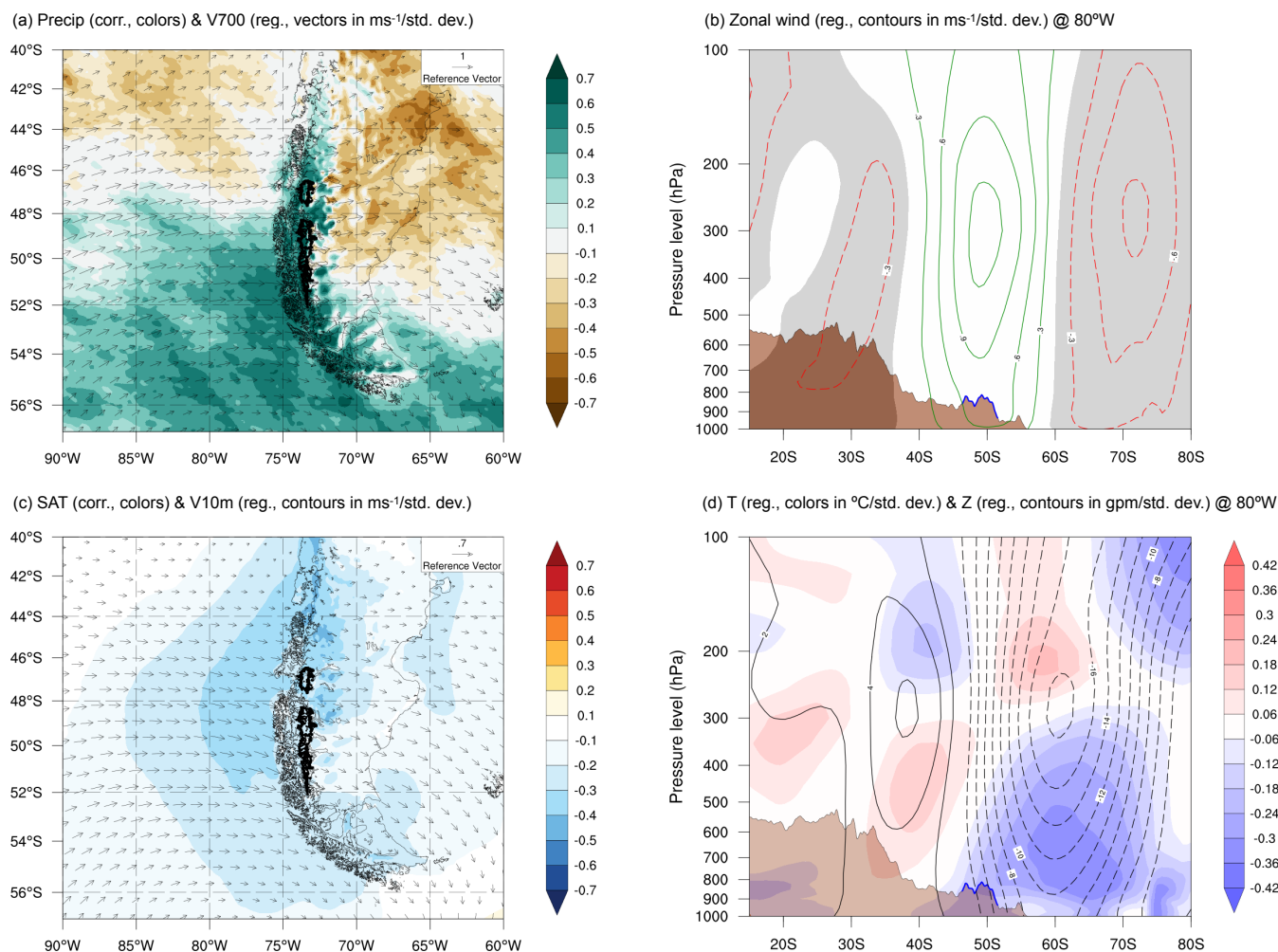
Figure 6. Regional correlation and linear regression maps of the annual (April to March) time series of the spatially averaged field of SMB with fields obtained from the RegCMv4 simulation data and ERA-Interim reanalysis. a) Regression with annual fields of horizontal wind at 700 hPa (vectors in ms^{-1}/std. dev.) and correlation with accumulated precipitation (colors). Fields were obtained from the RegCMv4 data. b) Latitudinal and atmospheric profile of the regression with annual field of zonal wind (contours in ms^{-1}/std. dev.) for a transect at 80 ºW. Negative regression values are shaded, and the Andes topography within the latitudinal band of the Patagonian Icefields is shown with blue lines. Fields were obtained from the ERA-Interim reanalysis. c) Regression with annual fields of horizontal wind at 10 m above ground level (vectors in ms^{-1}/std. dev.) and correlation with the mean near-surface air temperature (colors). Fields were obtained from the RegCMv4 data. d) Latitudinal and atmospheric profile of the regression with annual field of geopotential height (contours in gpm/std. dev.) and temperature (colors in ºC/std. dev.) for a transect at 80 ºW. Negative regression values are shaded, and the Andes topography within the latitudinal band of the Patagonian Icefields is shown with blue lines. Fields were obtained from the ERA-Interim reanalysis.

Annual SMB projected onto winter fields of selected variables

(a) Precip (corr., colors) & V700 (reg., vectors in ms⁻¹/std. dev.)

(b) Zonal wind (reg., contours in ms⁻¹/std. dev.) @ 80ºW

(c) SAT (corr., colors) & V10m (reg., contours in ms⁻¹/std. dev.)

(d) T (reg., colors in ºC/std. dev.) & Z (reg., contours in gpm/std. dev.) @ 80ºW
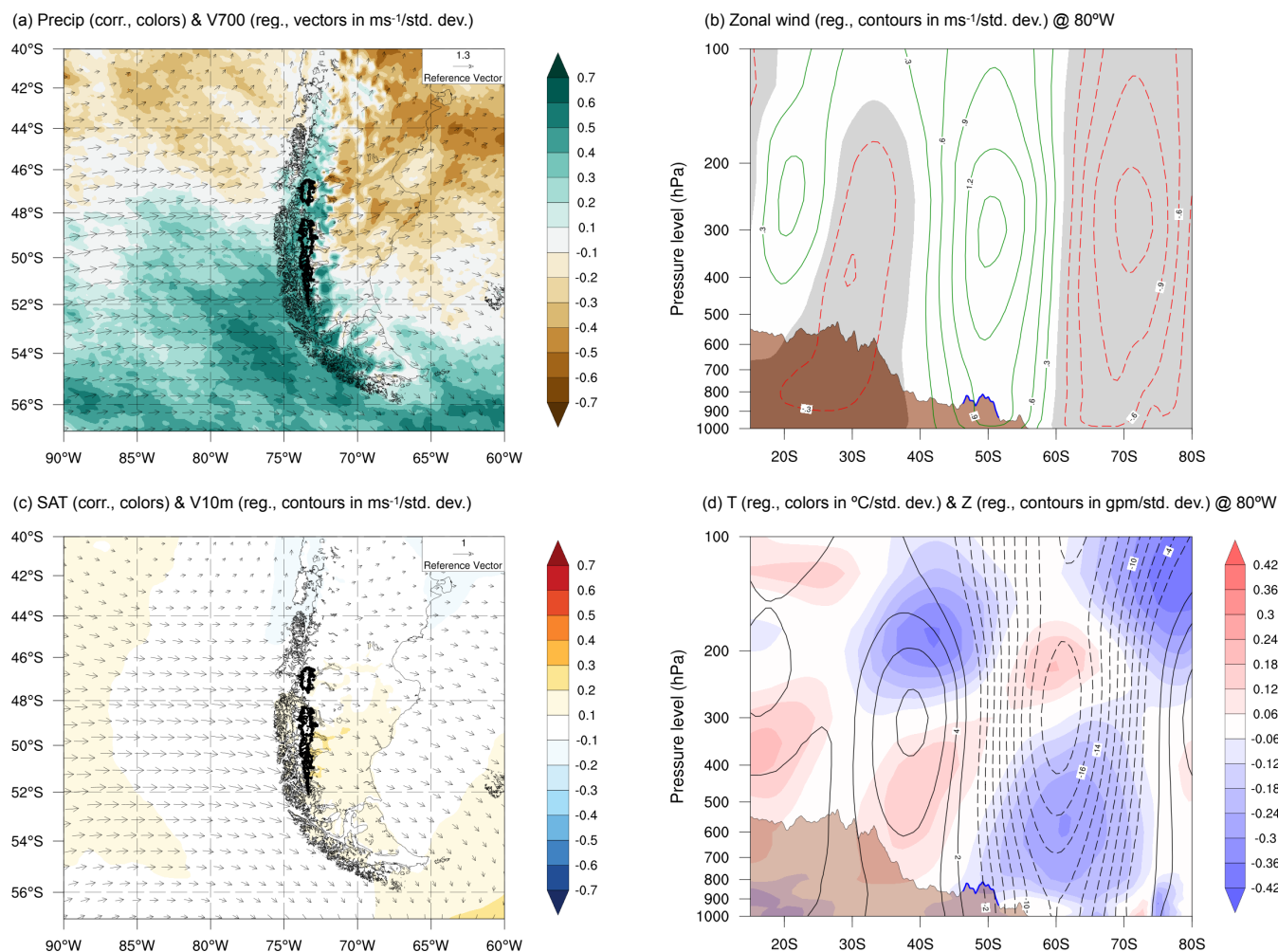
Figure 7. The same as in Fig. 6 but for the winter (April to September).

3.4 Large-scale control over the SMB

355 To assess the large-scale control over the SMB, we computed the regression fields of several climatic variables (at annual, winter, and summer timescales) onto the annual time series of the spatially averaged field of SMB. The results are shown in Figs. 9-11.

Years with SMB above the average are characterized by the presence of an anomalous low-pressure center located around the Drake Passage (hereafter Drake low) with a longitudinal extension from the northeastern Amundsen Sea and northeastern 360 Antarctic Peninsula (∼120ºW to 50ºW), and a latitudinal extension from the west Antarctic coast to the southern tip of South

Annual SMB projected onto summer fields of selected variables

(a) Precip (corr., colors) & V700 (reg., vectors in ms⁻¹/std. dev.)

(b) Zonal wind (reg., contours in ms⁻¹/std. dev.) @ 80°W

(c) SAT (corr., colors) & V10m (reg., contours in ms⁻¹/std. dev.)

(d) T (reg., colors in °C/std. dev.) & Z (reg., contours in gpm/std. dev.) @ 80°W
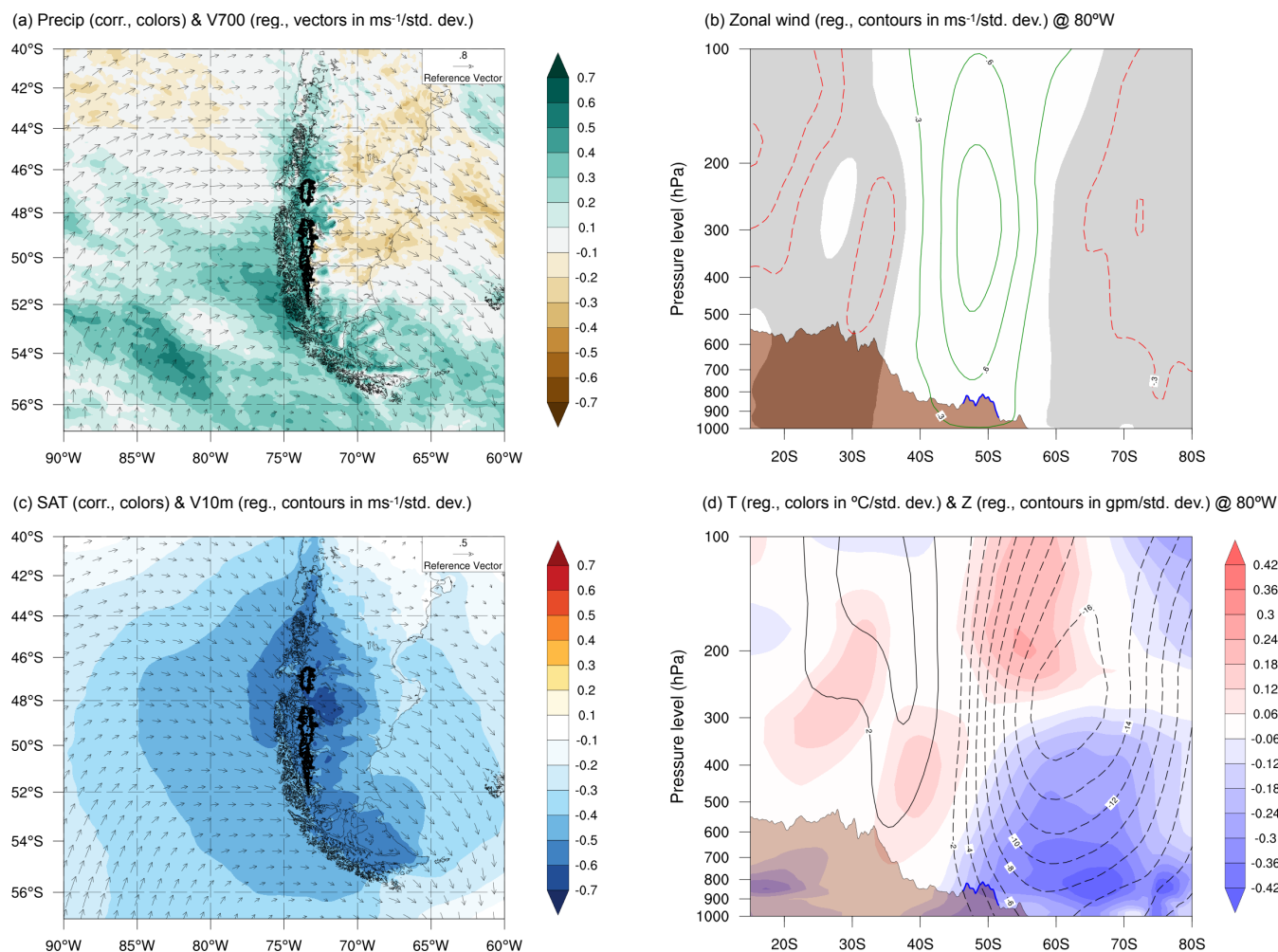
Figure 8. The same as in Fig. 6 but for the summer (October to March).

America (Fig. 9a). Around the Drake low, anomalous high-pressure centers are established over the subtropical South Pacific, extending towards the Amundsen Sea and the South Atlantic.

The Drake low is associated with an anomalous cyclonic circulation established around the Drake Passage (Fig. 9b). A strengthening of the annual zonal winds in the latitudinal band comprising the Patagonian Icefields and the longitudinal band comprising the 60-120 °W is observed, while a weakening of the zonal wind is exhibited southward. Furthermore, an intensification of the trade winds is also observed over the central equatorial Pacific, with magnitudes comparable to the ones exhibited by the westerly winds impinging the Patagonian Icefields.

365
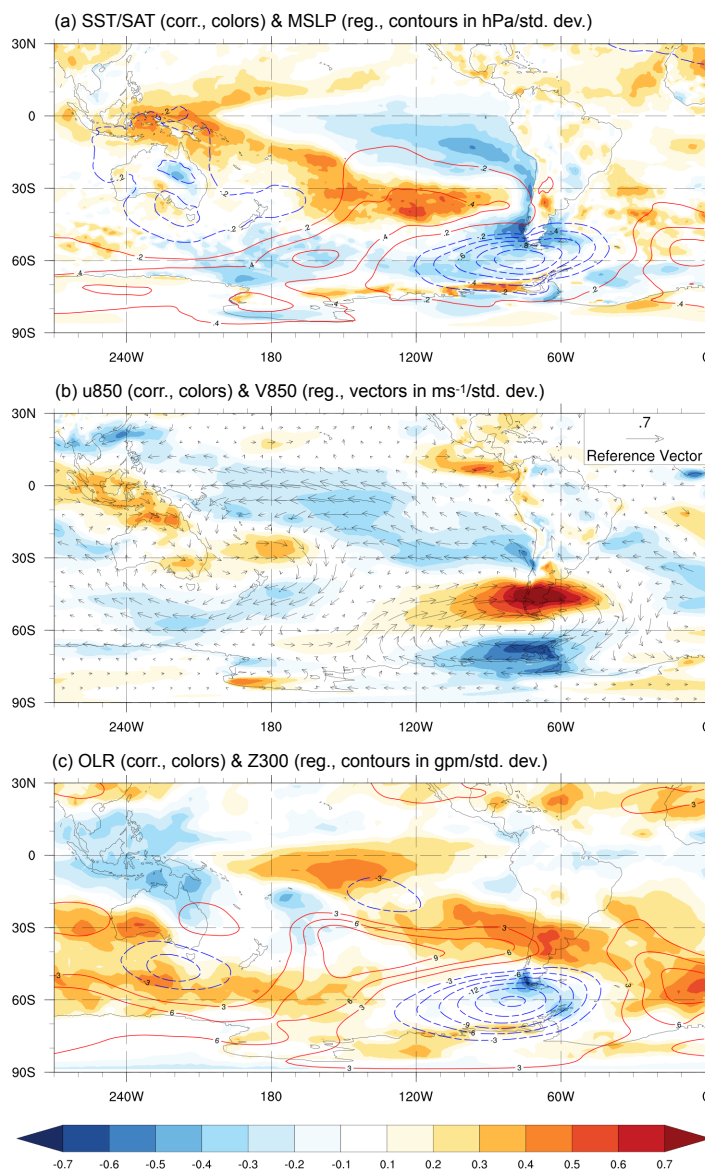
Figure 9. Large-scale correlation and linear regression maps of the annual (April to March) time series of the spatially averaged field of SMB with fields obtained from the Era-Interim reanalysis. a) Regression with the annual field of mean sea level pressure (contours in hPa/std. dev.) and correlation with the annual field of sea surface temperature (colors over ocean) and near-surface air temperature (colors over land). b) Regression with the annual field of horizontal wind at 850 hPa (vectors in ms^{-1}/std. dev.) and correlation with the annual field of zonal wind at 850 hPa (colors). c) Regression with the annual field of geopotential height at 300 hPa (contours in gpm/std. dev.) and correlation with the annual field of outgoing longwave radiation (colors).

Regarding SST anomalies, positive anomalies of annual SMB are associated with a surface cooling off the coast of Patagonia, in accordance with the regional-scale analysis (see Fig. 6). A large-scale cooling is observed around the central-eastern
370 equatorial Pacific and the west coast and southern tip of South America, resembling an Eastern Pacific La Niña-like pattern (Fig. S5). Nonetheless, this pattern is latitudinally asymmetric with respect to the equator, and the strongest SST correlations are associated with off-equatorial tongues off the coast of South America. In addition, beneath the anomalous cold tongue around the equatorial Pacific, an anomalous warm tongue emerges from the western equatorial Pacific towards the subtropical South Pacific.

375 Years with SMB above the average are associated with positive OLR anomalies over the central equatorial Pacific (i.e., decreased convective activity) and negative OLR anomalies over the western equatorial Pacific (Fig. 9c), consistent with the SST patterns. These OLR anomalies are accompanied by anomalies of geopotential height at 300 hPa that account for both (i) an equivalent barotropic arrangement of the Drake low, which extends throughout the troposphere, and (ii) a series of low, high and low anomalies pressures that appear to spread from the tropics to the extratropics as a result of inhibition of convective
380 activity over the central equatorial Pacific.

Concerning seasonal differences, years with SMB above the average are characterized by a deeper and more extensive Drake low during winter than summer and a more marked anomalous high-pressure signal to the north of the Patagonian Icefields as well (Figs. 10, 11). Moreover, a more pronounced enhancement of the westerly winds impinging Patagonia is evident during winter than summer, and the same occurs with the intensification of the trade winds in the central equatorial Pacific. Conversely,
385 the cooling signal over the western Patagonian coasts and the equatorial Pacific Ocean is much more intense during summer than the winter (Figs. 10a, 11a), and the OLR and geopotential height at 300 hPa anomalies are also much more evident during summer than winter (Figs. 10c, 11c).

3.5 Correlation with large-scale indices

Table 5 shows the correlation between indices of main modes of interannual variability affecting the Patagonian climate and
390 the time series of spatially averaged fields of SMB, accumulated precipitation, and near-surface temperature at annual, winter, and summer timescales. Additionally, we show the correlation with the custom indices described in Section 2.3.5.

Low correlations are found between the main modes of interannual variability affecting the Patagonian climate and the modeled time series. Our results show an almost null correlation between the CP index and the SMB time series at all timescales considered. A higher but still not statistically significant correlation is found between the EP index and the SMB time series at
395 annual timescale ($r = -0.33$) as well as winter ($r = -0.15$) and summer ($r = -0.15$) timescales. Regarding the SAM index, a very weak correlation was found between this index and the SMB time series at all timescales (see SAM pattern in Fig. S7).

High correlation values are found between the Z300 Drake index and the modeled time series. For instance, there is a strong and statistically significant correlation between Z300 Drake and the SMB time series at annual ($r = -0.65^*$), winter ($r = -0.66^*$), and summer ($r = -0.54^*$) timescales. Furthermore, the Z300 Drake index is highly correlated with the precipitation
400 time series at all timescales, while there is a statistically significant correlation with the temperature time series only in summer ($r = 0.42^*$). Additionally, the T850 Drake index shows a strong correlation with the SMB time series at all timescales and a

Annual SMB projected onto winter fields of selected variables
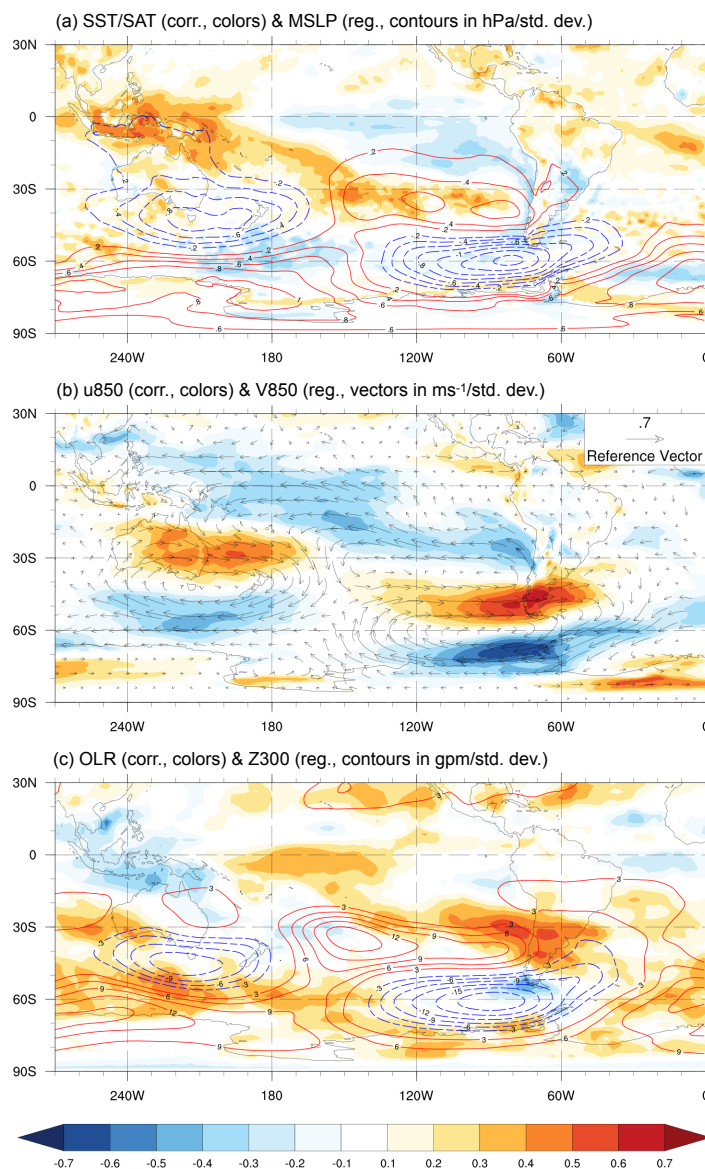
Figure 10. The same as in Fig. 9 but for the winter (April to September).

high correlation with the near-surface temperature time series during summer ($r = 0.63^*$). The highest correlation between the SMB time series and the set of indices explored is maintained with the U850-R3 index, at annual ($r = 0.71^*$), winter ($r = 0.85^*$), and summer ($r = 0.59^*$) timescales.

405   Finally, there is a strong coherence between the Z300 Drake index and the T850 Drake index at annual ($r = 0.79^*$), winter ($r = 0.76^*$), and summer ($r = 0.86^*$) timescales. Also, we found a good correlation between the SST-R2 index and the T850
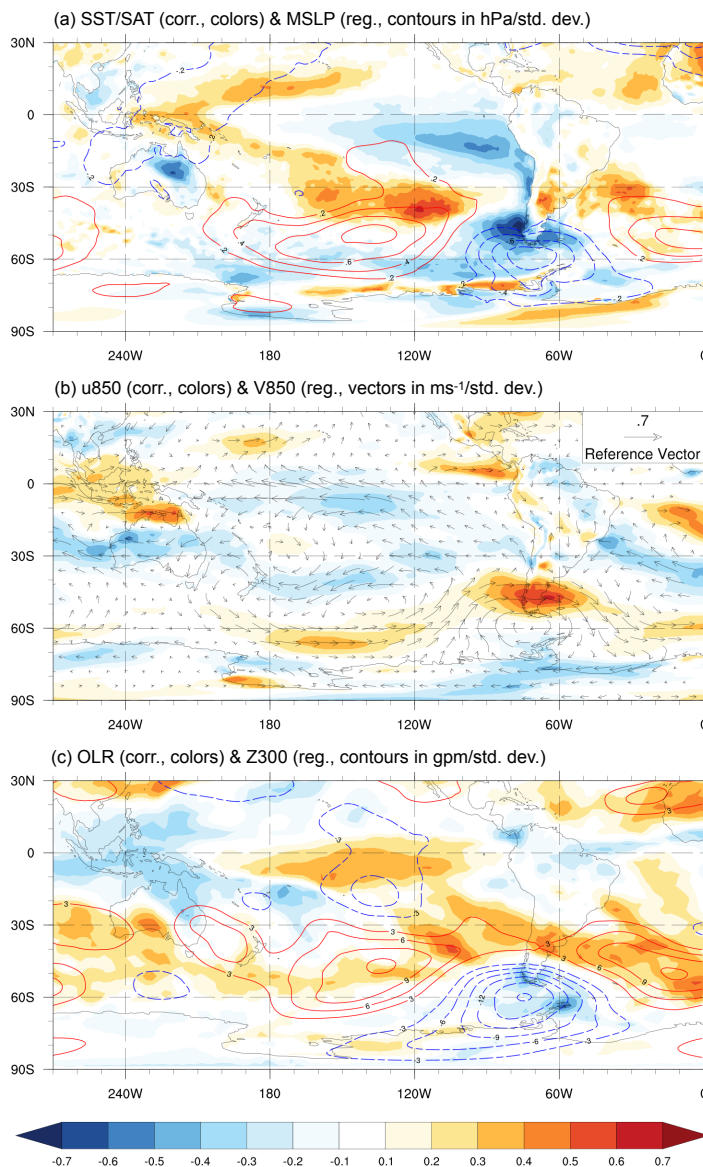
Figure 11. The same as in Fig. 9 but for the summer (October to March).

Drake index at annual ($r = 0.49^*$) and summer ($r = 0.76^*$) timescales, and also a good correlation between the Z300 Drake index and the U850-R3 index at all timescales ($|r| > 0.73^*$).

	Annual correlation			Winter correlation			Summer correlation		
	SMB	PRECIP	TEMP	SMB	PRECIP	TEMP	SMB	PRECIP	TEMP
Nino 3.4	−0.20	−0.32	−0.08	−0.10	−0.07	−0.08	−0.09	−0.38*	−0.12
Nino 1+2	−0.27	−0.25	0.04	−0.12	0.00	0.10	−0.14	−0.37*	−0.03
EP ENSO	−0.33	−0.24	0.04	−0.15	−0.02	0.12	−0.15	−0.20	0.07
CP ENSO	−0.04	−0.16	−0.05	0.02	−0.06	−0.16	−0.03	−0.20	−0.05
SAM	−0.08	0.10	0.26	−0.12	−0.01	0.18	−0.12	0.01	0.07
Z300 Drake	−0.65*	−0.60*	0.07	−0.66*	−0.65*	−0.15	−0.54*	−0.48*	0.42*
T850 Drake	−0.67*	−0.38*	0.46*	−0.46*	−0.29	0.32	−0.63*	−0.34	0.63*
SST-R2	−0.57*	−0.20	0.41*	−0.24	0.00	0.34*	−0.66*	−0.25	0.68*
U850-R3	0.71*	0.86*	0.26	0.85*	0.92*	0.52*	0.59*	0.80*	−0.15

Table 5. Correlation between indices of the main modes of interannual variability influencing Patagonia (and other custom indices) and the time series of spatially average fields of SMB, accumulated precipitation and mean temperature. (*) Statistically significant value at a significance level of 5%.

4 Discussion

410   The present study was designed to assess the present-day climatic control of the SMB of the Patagonian Icefields at interannual timescales. We modeled the meteorological and glaciological conditions over the Patagonian Icefields to obtain a time series of spatially averaged fields of SMB, precipitation, near-surface temperature, and other variables. We calibrated the parameters of the SMB model so that we could obtain similar values of mean annual SMB for the NPI and the SPI to those found in Minowa et al. (2021). The meteorological forcing of the SMB model was modified to ensure that possible biases in the mean value

415   of precipitation and temperature do not change our main results and conclusions. In this way, we considered the uncertainty related to the amount of precipitation that falls in Patagonia and the Patagonian Icefields (Sauter, 2020; Bravo et al., 2021), and we did the same for temperature.

The sensitivity experiment allowed us to rule out the solar radiation as a possible controlling variable of the SMB. The experiment showed that precipitation exerts the primary control over the SMB, followed by temperature. This outcome is

420   consistent with the regression analysis results at the local scale by which annual anomalies in the SMB are related primarily to anomalies in accumulation (highly correlated to precipitation) and secondarily to anomalies in ablation (highly correlated to temperature). While accumulation anomalies are expected to dominate during winter and summer, ablation anomalies are significant only during summer. Accordingly, the regression analysis at the local scale shows that years of relatively high SMB show an increase in annual precipitation (greater in winter) and a decrease in summer temperatures, while years of relatively

425 low SMB are related to the opposite conditions. We argue these as the most favorable local meteorological conditions to produce anomalies in the SMB signal.

As our principal finding, we found a strong connection between the SMB of the Patagonian Icefields and the sea level pressure near the Drake Passage at interannual timescales. Based on our results, we propose that years of relatively high SMB are characterized by the presence of the Drake low (Fig 9a) that induces an enhancement of the westerlies impinging the

430 Patagonian Icefields. This, in turn, increases the precipitation via orographic enhancement (Roe, 2005; Garreaud et al., 2013). The Drake low is thermodynamically maintained by a core of cold air that concurrently cools the Patagonian Icefields and the Pacific Ocean adjacent to Patagonia (Fig. 6d), especially in summer (Fig. 8d) when this core is cooler and further north than that in winter (Fig. 7d). We hypothesize that during winter, even if no cooling occurs, the core of cold air prevents the warming associated with increased zonal winds in central Patagonia that would otherwise be expected under normal conditions

435 (Garreaud et al., 2013, see Table 5). In addition, during winter, the meridional gradient of geopotential height (Z300, Fig. 10c) to the west of Patagonia tends to be stronger than that during summer (Fig. 11c) due to a more pronounced high-pressure anomaly established over the subtropical Andes. This produces a greater increase in westerly winds and precipitation during winter than in summer (Figs. 7, 8). In this way, both the dynamics and thermodynamics associated with the Drake low would explain the increase in annual precipitation (greater in winter) and the decrease in summer temperature associated with years

440 of relatively high SMB.

We found only weak correlations between the SMB and atmospheric modes of variability, such as the El Niño-Southern Oscillation (ENSO) and the Southern Annular Mode (SAM), implying little dependency between these modes and the SMB of the Patagonian Icefields (Table 5). We highlight that this result characterizes the present-day long-term (1980-2015) linear relationship between the annual variability of atmospheric modes and the SMB. One single event may profoundly impact the

445 mass balance of the Patagonian Icefields (see for example Gómez et al. (2022)), which agrees with our results as long as the long-term linear relationship maintains weak. Our results suggest that the low (high) pressure anomalies located over the Amundsen-Bellingshausen Sea during Central Pacific La Niña (El Niño) events (see Yuan et al. (2018) and references therein; also see our Fig. S6) are ineffective to enhance (reduce) the westerlies impinging the Patagonian Icefields due to westward displacement of the anomalous pressure center from the Drake Passage. Meanwhile, even though Eastern Pacific La Niña

450 (El Niño) events are associated with the presence of low (high) pressure center anomalies near the Drake passage (Fig. S5), these anomalies appear to be much stronger during years of relatively high SMB than during years of relatively low EP index. Anyhow, the specific reasons why Eastern Pacific La Niña events are ineffective to produce years of relatively high SMB require further investigation. On the other hand, positive (negative) SAM phases exhibit slight strengthening (weakening) of the westerlies upstream of Patagonian Icefields and simultaneous anomalous warming (cooling) of Patagonia (Fig. S7). This

455 means that for the SAM index the two observed processes tend to cancel each other out in developing SMB anomalies.

This study does not assess the teleconnections that potentially trigger the Drake low. However, we speculate that the origin of this pressure feature might be associated with tropical forcing due to the decreased convective activity over the central equatorial Pacific and increased convective activity over the western equatorial Pacific observed during years of relatively high SMB (Fig 9c). As the SMB correlates better to the Eastern Pacific ENSO index than the Central Pacific ENSO index (Table

460 5), we argue that the establishment of the Drake low would be highly sensitive to the specific location of SST anomalies in the tropical Pacific. The low correlation between the Eastern Pacific ENSO index and the SMB could be a consequence of similar considerations that only certain eastern Pacific SST warming and cooling events could activate an anomalous pressure center near the Drake Passage. Additionally, we conjecture that the summer cooling of the Patagonian Icefields during years of relatively high SMB is mainly associated with the thermodynamics of the Drake low, as exposed previously, and not with

465 the eastern Pacific SST cooling. This seems reasonable since nearly 40% of the variance of the summer temperature over the Patagonian icefields is explained by the lower tropospheric temperature near the Drake Passage (Table 5).

5   Conclusions

In this study, we investigated the present-day climatic control of the SMB of the Patagonian Icefields through the modeling of its main surface meteorological and glaciological conditions during the period 1980-2015. We assessed the modeled fields and

470 their covariability with other climate fields as well as main atmospheric modes of variability at the interannual timescale to determine the local- and large-scale climate processes controlling the annual SMB variations of the Patagonian Icefields. Our main findings are as follows:

- The interannual SBM variability of the Patagonian Icefields is controlled by the precipitation and near-surface temperature variabilities. Year-to-year SMB variations show almost no dependence on downward surface solar radiation

475 variations.

- Regarding the local scale conditions, years of relatively high SMB are characterized by higher than average annual accumulation and lower than average summer ablation. In turn, these conditions are associated with wetter than average annual and cooler than average summer conditions due to the fact accumulation (ablation) is highly correlated with precipitation (temperature). Opposite conditions are evident during the years with lower than average SMB.

480 - In relation to the regional scale conditions, higher than average SMB years are characterized by an intensification of the westerly winds impinging the Patagonian Icefields and an increase of the precipitation in western Patagonia accompanied with relatively dry dryer conditions to the east of the Andes ridge. Higher than average SMB years indicate a regional decrease in summer near-surface temperatures, while no or little winter temperature changes are evident. Years with relatively low SMB show the opposite conditions.

485 - Concerning the large-scale conditions, years of relatively high SMB characterized by the establishment of an anomalous low- pressure center near the Drake Passage, the Drake low, that induces an anomalous cyclonic circulation accompanied with enhanced westerlies impinging the Patagonian Icefields. The Drake low is thermodynamically maintained by a core of cold air that cools the Patagonian Icefields during summer. Years with lower than average SMB are associated with the opposite conditions.

490   – We found little dependency between the interannual SBM variability of the Patagonian Icefields and main atmospheric
modes of variabilities such as SAM and warm and cold ENSO phases. Further work is required to understand the low
annual correlation between EP ENSO index and the SMB of the Patagonian Icefields.

This research study gives new insights for understanding the complex interplay between the present-day climate processes
and local-scale cryospheric processes in the southern Andean Cordillera. Low dependence of the Patagonian Icefields' SMB
495   on main atmospheric modes of variability suggests a poor ability of ENSO and SAM indexes to reproduce the past and future
interannual variability of the SMB. Instead, this study highlights the Drake Passage as a key region capable of reproducing
the interannual variability of the SMB since it explains the linkage between large-scale processes and the SMB behavior
reasonably. Finally, findings from local-scale assessment facilitate the diagnostic of SMB anomalies in terms of precipitation,
near-surface air temperature, and surface downward solar radiation anomalies, providing a conceptual framework useful for
500   future research in the area.

Author contributions. TC conducted the investigation with the supervision of MR and RG. All co-authors contributed to the conceptualiza-
tion of the research goals. TC implemented the model code, performed the simulations and prepared the manuscript with contributions from
all co-authors.

Competing interests. The authors declare that they have no conflict of interest.

505   *Acknowledgements.* This research emerged from the leading author's master thesis project funded by the Chilean National Agency for
Research and Development (CONICYT-PCHA/MagísterNacional/2016-22160660). We also thank to the Center for Climate and Resilience
Research (CR2, CONICYT/FONDAP/15110009) for supporting with data and equipment to carry out this work, and for providing partial
funding.

References

510   Agosta, E. A., Hurtado, S. I., and Martin, P. B.: "Easterlies"-induced precipitation in eastern Patagonia: Seasonal influences of ENSO'S
FLAVOURS and SAM, International Journal of Climatology, 40, 5464–5484, 2020.

Alvarez-Garreton, C., Mendoza, P. A., Boisier, J. P., Addor, N., Galleguillos, M., Zambrano-Bigiarini, M., Lara, A., Puelma, C., Cortes, G.,
Garreaud, R., et al.: The CAMELS-CL dataset: catchment attributes and meteorology for large sample studies–Chile dataset, Hydrology
and Earth System Sciences, 22, 5817–5846, 2018.

515   Aniya, M.: Glacier inventory for the Northern Patagonia Icefield, Chile, and variations 1944/45 to 1985/86, Arctic and Alpine Research, 20,
179–187, 1988.

Aniya, M., Naruse, R., Casassa, G., and Rivera, A.: Variations of Patagonian glaciers, South America, utilizing RADARSAT images, in:
Proceedings of the International Symposium on RADARSAT Application Development and Research Opportunity (ADRO), Montreal,
Canada, vol. 1315, 1998.

520   Aravena, J.-C. and Luckman, B. H.: Spatio-temporal rainfall patterns in southern South America, International Journal of Climatology: A
Journal of the Royal Meteorological Society, 29, 2106–2120, 2009.

Arblaster, J. M. and Meehl, G. A.: Contributions of external forcings to southern annular mode trends, Journal of climate, 19, 2896–2905,
2006.

Berbery, E. H. and Vera, C. S.: Characteristics of the Southern Hemisphere winter storm track with filtered and unfiltered data, Journal of the
525   Atmospheric Sciences, 53, 468–481, 1996.

Boisier, J. P., Alvarez-Garreton, C., Cordero, R. R., Damiani, A., Gallardo, L., Garreaud, R. D., Lambert, F., Ramallo, C., Rojas, M.,
Rondanelli, R., et al.: Anthropogenic drying in central-southern Chile evidenced by long-term observations and climate model simulations,
Elementa: Science of the Anthropocene, 6, 2018.

Bozkurt, D., Rojas, M., Boisier, J. P., Rondanelli, R., Garreaud, R., and Gallardo, L.: Dynamical downscaling over the complex terrain of
530   southwest South America: present climate conditions and added value analysis, Climate Dynamics, 53, 6745–6767, 2019.

Braun, M. H., Malz, P., Sommer, C., Farías-Barahona, D., Sauter, T., Casassa, G., Soruco, A., Skvarca, P., and Seehaus, T. C.: Constraining
glacier elevation and mass changes in South America, Nature Climate Change, 9, 130–136, 2019.

Bravo, C., Bozkurt, D., Ross, A. N., and Quincey, D. J.: Projected increases in surface melt and ice loss for the Northern and Southern
Patagonian Icefields, Scientific Reports, 11, 1–13, 2021.

535   Cai, W., McPhaden, M. J., Grimm, A. M., Rodrigues, R. R., Taschetto, A. S., Garreaud, R. D., Dewitte, B., Poveda, G., Ham, Y.-G., Santoso,
A., et al.: Climate impacts of the El Niño–southern oscillation on South America, Nature Reviews Earth & Environment, 1, 215–231,
2020.

Capotondi, A., Wittenberg, A. T., Newman, M., Di Lorenzo, E., Yu, J.-Y., Braconnot, P., Cole, J., Dewitte, B., Giese, B., Guilyardi, E., et al.:
Understanding ENSO diversity, Bulletin of the American Meteorological Society, 96, 921–938, 2015.

540   Carrasco, J. F., Casassa, G., and Rivera, A.: Meteorological and climatological aspects of the Southern Patagonia Icefield, in: The Patagonian
Icefields, pp. 29–41, Springer, 2002.

Carrasco-Escaff, T.: Evaluación del control atmosférico sobre el balance de masa superficial de los campos de hielo patagóni-
cos en el clima presente usando modelación, Master's thesis, Departamento de Geofísica, Universidad de Chile, Santiago, Chile,
https://repositorio.uchile.cl/handle/2250/181576, 2021.

545   Casassa, G., Rodríguez, J. L., and Loriaux, T.: A new glacier inventory for the Southern Patagonia Icefield and areal changes 1986–2000, in: Global land ice measurements from space, pp. 639–660, Springer, 2014.

Cuffey, K. M. and Paterson, W. S. B.: The physics of glaciers, Academic Press, 2010.

Dee, D. P., Uppala, S. M., Simmons, A. J., Berrisford, P., Poli, P., Kobayashi, S., Andrae, U., Balmaseda, M., Balsamo, G., Bauer, d. P., et al.: The ERA-Interim reanalysis: Configuration and performance of the data assimilation system, Quarterly Journal of the royal meteorological

550   society, 137, 553–597, 2011.

Demortier, A., Bozkurt, D., and Jacques-Coper, M.: Identifying key driving mechanisms of heat waves in central Chile, Climate Dynamics, 57, 2415–2432, 2021.

Dussaillant, A., Buytaert, W., Meier, C., and Espinoza, F.: Hydrological regime of remote catchments with extreme gradients under accelerated change: the Baker basin in Patagonia, Hydrological sciences journal, 57, 1530–1542, 2012.

555   Dussaillant, I., Berthier, E., and Brun, F.: Geodetic mass balance of the Northern Patagonian Icefield from 2000 to 2012 using two independent methods, Frontiers in Earth Science, 6, 8, 2018.

Dussaillant, I., Berthier, E., Brun, F., Masiokas, M., Hugonnet, R., Favier, V., Rabatel, A., Pitte, P., and Ruiz, L.: Two decades of glacier mass loss along the Andes, Nature Geoscience, 12, 802–808, 2019.

Fogt, R. L. and Marshall, G. J.: The Southern Annular Mode: variability, trends, and climate impacts across the Southern Hemisphere, Wiley

560   Interdisciplinary Reviews: Climate Change, 11, e652, 2020.

Foresta, L., Gourmelen, N., Weissgerber, F., Nienow, P., Williams, J., Shepherd, A., Drinkwater, M. R., and Plummer, S.: Heterogeneous and rapid ice loss over the Patagonian Ice Fields revealed by CryoSat-2 swath radar altimetry, Remote Sensing of Environment, 211, 441–455, 2018.

Garreaud, R.: Record-breaking climate anomalies lead to severe drought and environmental disruption in western Patagonia in 2016, Climate

565   Research, 74, 217–229, 2018.

Garreaud, R., Lopez, P., Minvielle, M., and Rojas, M.: Large-scale control on the Patagonian climate, Journal of Climate, 26, 215–230, 2013.

Garreaud, R. D., Vuille, M., Compagnucci, R., and Marengo, J.: Present-day south american climate, Palaeogeography, Palaeoclimatology, Palaeoecology, 281, 180–195, 2009.

Gillett, N. P. and Thompson, D. W.: Simulation of recent Southern Hemisphere climate change, Science, 302, 273–275, 2003.

570   Gómez, D. D., Bevis, M. G., Smalley, R., Durand, M., Willis, M. J., Caccamise, D. J., Kendrick, E., Skvarca, P., Sobrero, F. S., Parra, H., et al.: Transient ice loss in the Patagonia Icefields during the 2015–2016 El Niño event, Scientific Reports, 12, 1–8, 2022.

González-Reyes, Á., Aravena, J. C., Muñoz, A. A., Soto-Rogel, P., Aguilera-Betti, I., and Toledo-Guerrero, I.: Variabilidad de la precipitación en la ciudad de Punta Arenas, Chile, desde principios del siglo XX, in: Anales del Instituto de la Patagonia, vol. 45, pp. 31–44, Universidad de Magallanes, 2017.

575   Hoskins, B. J. and Hodges, K. I.: A new perspective on Southern Hemisphere storm tracks, Journal of Climate, 18, 4108–4129, 2005.

Hoskins, B. J. and Karoly, D. J.: The steady linear response of a spherical atmosphere to thermal and orographic forcing, Journal of the Atmospheric Sciences, 38, 1179–1196, 1981.

Jaber, W. A., Floricioiu, D., and Rott, H.: Geodetic mass balance of the Patagonian Icefields derived from SRTM and TanDEM-X data, in: 2016 IEEE International Geoscience and Remote Sensing Symposium (IGARSS), pp. 342–345, IEEE, 2016.

580   Jacques-Coper, M., Brönnimann, S., Martius, O., Vera, C., and Cerne, B.: Summer heat waves in southeastern Patagonia: an analysis of the intraseasonal timescale, International journal of climatology, 36, 1359–1374, 2016.

Jobbágy, E. G., Paruelo, J. M., and León, R. J.: Estimación del régimen de precipitación a partir de la distancia a la cordillera en el noroeste de la Patagonia, Ecología Austral, 5, 047–053, 1995.

Kao, H.-Y. and Yu, J.-Y.: Contrasting eastern-Pacific and central-Pacific types of ENSO, Journal of Climate, 22, 615–632, 2009.

585 Karoly, D. J.: Southern hemisphere circulation features associated with El Niño-Southern Oscillation events, Journal of Climate, 2, 1239–1252, 1989.

Lee, H. and NOAA CDR Program: NOAA Climate Data Record (CDR) of Monthly Outgoing Longwave Radiation (OLR), Version 2.2-1 [Data set], NOAA National Climatic Data Center, doi:10.7289/V5222RQP [Accessed 2020-10-01], 2011.

Lenaerts, J. T., Van Den Broeke, M. R., van Wessem, J. M., van de Berg, W. J., van Meijgaard, E., van Ulft, L. H., and Schaefer, M.: Extreme

590 precipitation and climate gradients in Patagonia revealed by high-resolution regional atmospheric climate modeling, Journal of climate, 27, 4607–4621, 2014.

Malz, P., Meier, W., Casassa, G., Jaña, R., Skvarca, P., and Braun, M. H.: Elevation and mass changes of the Southern Patagonia Icefield derived from TanDEM-X and SRTM data, Remote Sensing, 10, 188, 2018.

Martínez-Harms, M. J. and Gajardo, R.: Ecosystem value in the Western Patagonia protected areas, Journal for Nature Conservation, 16,

595 72–87, 2008.

Mernild, S. H., Liston, G. E., Hiemstra, C., and Wilson, R.: The Andes Cordillera. Part III: glacier surface mass balance and contribution to sea level rise (1979–2014), International Journal of Climatology, 37, 3154–3174, 2017.

Minowa, M., Schaefer, M., Sugiyama, S., Sakakibara, D., and Skvarca, P.: Frontal ablation and mass loss of the Patagonian icefields, Earth and Planetary Science Letters, 561, 116 811, 2021.

600 Mo, K. C. and Higgins, R. W.: The Pacific–South American modes and tropical convection during the Southern Hemisphere winter, Monthly Weather Review, 126, 1581–1596, 1998.

Mo, K. C. and Paegle, J. N.: The Pacific–South American modes and their downstream effects, International Journal of Climatology: A Journal of the Royal Meteorological Society, 21, 1211–1229, 2001.

Montecinos, A. and Aceituno, P.: Seasonality of the ENSO-related rainfall variability in central Chile and associated circulation anomalies,

605 Journal of climate, 16, 281–296, 2003.

NASA JPL: NASA Shuttle Radar Topography Mission Global 3 arc second sub-sampled [Data set], NASA EOSDIS Land Processes DAAC, accessed 2020-10-01 from https://doi.org/10.5067/MEaSUREs/SRTM/SRTMGL3S.003, 2013.

Oerlemans, J.: Glaciers and climate change, CRC Press, 2001.

Olivares-Contreras, V., Mattar, C., Gutiérrez, A. G., and Jiménez, J.: Warming trends in Patagonian subantartic forest, International Journal

610 of Applied Earth Observation and Geoinformation, 76, 51–65, 2019.

Paruelo, J. M., Beltrán, A., Jobbágy, E., Sala, O. E., and Golluscio, R. A.: The climate of Patagonia: general patterns and controls on biotic processes, Ecología austral, 8, 085–101, 1998.

Quintana, J. and Aceituno, P.: Changes in the rainfall regime along the extratropical west coast of South America (Chile): 30-43° S, Atmósfera, 25, 1–22, 2012.

615 Rasmussen, L., Conway, H., and Raymond, C.: Influence of upper air conditions on the Patagonia icefields, Global and Planetary Change, 59, 203–216, 2007.

RGI Consortium: Randolph glacier inventory–a dataset of global glacier outlines: Version 6.0, Boulder, Colorado USA. NSIDC: National Snow and Ice Data Center, doi: https://doi.org/10.7265/4m1f-gd79, 2017.

Rignot, E., Rivera, A., and Casassa, G.: Contribution of the Patagonia Icefields of South America to sea level rise, Science, 302, 434–437,
620   2003.

Rivera, A., Benham, T., Casassa, G., Bamber, J., and Dowdeswell, J. A.: Ice elevation and areal changes of glaciers from the Northern
        Patagonia Icefield, Chile, Global and Planetary Change, 59, 126–137, 2007.

Roe, G. H.: Orographic precipitation, Annu. Rev. Earth Planet. Sci., 33, 645–671, 2005.

Rogers, J. C. and Van Loon, H.: Spatial variability of sea level pressure and 500 mb height anomalies over the Southern Hemisphere, Monthly
625   Weather Review, 110, 1375–1392, 1982.

Rosenblüth, B., Fuenzalida, H. A., and Aceituno, P.: Recent temperature variations in southern South America, International Journal of
        Climatology: A Journal of the Royal Meteorological Society, 17, 67–85, 1997.

Rutllant, J. and Fuenzalida, H.: Synoptic aspects of the central Chile rainfall variability associated with the Southern Oscillation, International
        Journal of Climatology, 11, 63–76, 1991.

630 Sauter, T.: Revisiting extreme precipitation amounts over southern South America and implications for the Patagonian Icefields, Hydrology
        and Earth System Sciences, 24, 2003–2016, 2020.

Schaefer, M., Machguth, H., Falvey, M., and Casassa, G.: Modeling past and future surface mass balance of the Northern Patagonia Icefield,
        Journal of Geophysical Research: Earth Surface, 118, 571–588, 2013.

Schaefer, M., Machguth, H., Falvey, M., Casassa, G., and Rignot, E.: Quantifying mass balance processes on the Southern Patagonia Icefield,
635   The Cryosphere, 9, 25–35, 2015.

Schneider, C. and Gies, D.: Effects of El Niño–southern oscillation on southernmost South America precipitation at 53 S revealed from
        NCEP–NCAR reanalyses and weather station data, International Journal of Climatology: A Journal of the Royal Meteorological Society,
        24, 1057–1076, 2004.

Taschetto, A. S., Ummenhofer, C. C., Stuecker, M. F., Dommenget, D., Ashok, K., Rodrigues, R. R., and Yeh, S.-W.: ENSO atmospheric
640   teleconnections, El Niño Southern Oscillation in a changing climate, pp. 309–335, 2020.

Thompson, D. W. and Wallace, J. M.: Annular modes in the extratropical circulation. Part I: Month-to-month variability, Journal of climate,
        13, 1000–1016, 2000.

Timmermann, A., An, S.-I., Kug, J.-S., Jin, F.-F., Cai, W., Capotondi, A., Cobb, K. M., Lengaigne, M., McPhaden, M. J., Stuecker, M. F.,
        et al.: El Niño–southern oscillation complexity, Nature, 559, 535–545, 2018.

645 Trenberth, K. E.: Storm tracks in the Southern Hemisphere, Journal of Atmospheric Sciences, 48, 2159–2178, 1991.

Wang, C., Deser, C., Yu, J.-Y., DiNezio, P., and Clement, A.: El Niño and southern oscillation (ENSO): a review, Coral reefs of the eastern
        tropical Pacific, pp. 85–106, 2017.

Warren, C. R. and Sugden, D. E.: The Patagonian icefields: a glaciological review, Arctic and Alpine Research, 25, 316–331, 1993.

Weidemann, S. S., Sauter, T., Kilian, R., Steger, D., Butorovic, N., and Schneider, C.: A 17-year record of meteorological observations across
650   the gran campo nevado ice cap in southern patagonia, Chile, related to synoptic weather types and climate modes, Frontiers in Earth
        Science, 6, 53, 2018.

Willis, M. J., Melkonian, A. K., Pritchard, M. E., and Ramage, J. M.: Ice loss rates at the Northern Patagonian Icefield derived using a decade
        of satellite remote sensing, Remote Sensing of Environment, 117, 184–198, 2012a.

Willis, M. J., Melkonian, A. K., Pritchard, M. E., and Rivera, A.: Ice loss from the Southern Patagonian ice field, South America, between
655   2000 and 2012, Geophysical research letters, 39, 2012b.

Yu, J.-Y., Zou, Y., Kim, S. T., and Lee, T.: The changing impact of El Niño on US winter temperatures, Geophysical Research Letters, 39, 2012.

Yuan, X., Kaplan, M. R., and Cane, M. A.: The interconnected global climate system—A review of tropical–polar teleconnections, Journal of Climate, 31, 5765–5792, 2018.

660   Zemp, M., Huss, M., Thibert, E., Eckert, N., McNabb, R., Huber, J., Barandun, M., Machguth, H., Nussbaumer, S. U., Gärtner-Roer, I., et al.: Global glacier mass changes and their contributions to sea-level rise from 1961 to 2016, Nature, 568, 382–386, 2019.